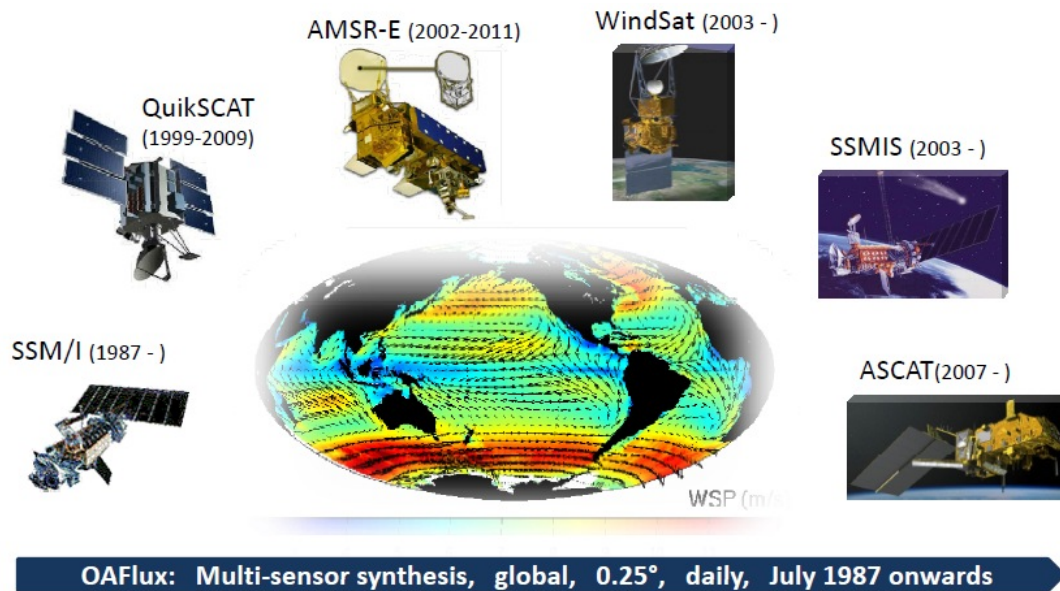




OAFlux High-Resolution Ocean-Surface Vector Wind Analysis Synergized from Satellite Scatterometers and Radiometers Part I: Methodology, Approach, and Challenging Issues

Lisan Yu and Xiangze Jin



OAFlux Project Technical Report No. OA-2013-01
July 2013

Preface

A high-resolution global analysis of daily ocean-surface vector winds that covers the entire satellite wind observing period, from the first launch of SSMI in July 1987 to the present, was developed by the Objectively Analyzed air-sea Heat Fluxes (OAFlux) project. The OAFlux vector wind analysis is a synergy of 12 satellite sensors that includes 2 scatterometers (QuikSCAT and ASCAT), and 10 passive microwave radiometers (AMSRE, 6 SSMI sensors, 2 SSMIS sensors, and the passive polarimetric microwave radiometer from WindSat).

A four-part report series was prepared, aiming to provide a systematic and conceptually organized review of the 12-sensor synergy and to support the public release of the datasets. Part I focuses on the methodology, approaches, and challenging technical issues in developing the multi-sensor synthesis. Part II documents the approach of error estimation that is developed to address the confidence and sensitivity of the OAFlux time series. Part III includes buoy-based validation. Part IV presents OAFlux time-mean fields of near-surface ocean vector winds and associated uncertainty estimates. The report series were developed from three research papers that were produced during the course of data development.

The datasets are freely available to interested users for non-commercial scientific research. For further information, please visit the project website at <http://oaflux.whoi.edu/> or contact the project PI (lyu@whoi.edu). The project is sponsored by the NASA Ocean Vector Wind Science Team (OVWST) activities. We sincerely thank the NASA support and technical input given by the international OVWST community during the four-year development.

Project PI: Lisan Yu
Woods Hole Oceanographic Institution

Abstract

Climate studies need more than ever a consistent long-term record of ocean-surface vector winds, as winds are virtually involved in every aspect of air-sea feedback and interaction. QuikSCAT (1999-2009) has so far provided the longest record of global scatterometer data yet obtained, and any effort made in extending the QuikSCAT period will inevitably invoke the synergy of QuikSCAT with sensors from different platforms. This study reports an objective synthesis of 12 satellite sensors that included 2 scatterometers and 10 passive microwave radiometers to produce a high-resolution ocean-surface vector wind time series from 1987 onward.

This part one technical report provided an insight on the theory of the synergy between scatterometers and radiometers and the practical use of the least-variance linear statistical estimation to combine multiple satellite sensors from multiple platforms. It is found that the most challenging issue in the multi-sensor synthesis is the construction of the near-surface circulation associated with synoptic weather storms due to three factors: (i) the lack of radiometer retrievals when rain presents, (ii) the elimination of rain-flagged QuikSCAT wind vector cells that lead to gappy satellite observations of the storm, and (iii) the persistent difference between QuikSCAT and ASCAT high winds. It is found that 98% of global daily wind can be estimated confidently from scatterometer and radiometer retrievals, while about 2% daily winds are influenced by rain and high winds and their estimates may have uncertainty. The study showed that objective synthesis is a viable platform for merging the advantages of sensors from different platforms.

This study is developed from the research paper entitled “A satellite-derived high-resolution ocean-surface vector wind analysis (1987 onward). Part I: Insight on the synergy between scatterometers and microwave radiometers”.

Key words: remote sensing, climate record of ocean-surface vector wind, scatterometer, passive microwave radiometer, mesoscale air-sea interaction

Table of Contents

Preface	2
Abstract	3
1. Introduction	7
2. Input satellite sensors	9
2.1 Type of wind sensors used in the OAFlux synthesis	9
2.2 Processing and quality-check satellite retrievals	13
3. Rationale supporting the synergy between scatterometers and radiometers	15
3.1 A theoretical perspective	15
3.2 Evidence from active and passive sensor retrievals	17
3.3 Global wind distribution in the low, moderate, and high wind categories	18
4. Methodology and strategy of synthesis	19
4.1 Methodology	19
4.2 Weight assignment	22
5. Challenging issues for the multi-sensor synthesis	24
5.1 Selection of resolution.....	24
5.2 Data gap filling.....	25
5.3 Sensitivity of daily-mean field to heavy rain associated with strong storms	27
5.4 Sensitivity of daily-mean field to high winds and rain on the global scale	30
5.5 Sensitivity of the OAFlux time series to high winds	31
6. Validity of the OAFlux synthesized fields	31
6.1 Daily mean from scatterometers	32
6.2 Daily mean from the OAFlux synthesis	33

6.3 Daily-mean differences between OAFlux and atmospheric reanalyses.....	34
6.4 OAFlux and atmospheric reanalyses for the pre-QuikSCAT period	35
7. Summary	36
Acknowledgements	41
References	42
Figure Captions	52
Figures (18)	55

1. Introduction

The Objectively Analyzed air-sea Heat Fluxes (OAFlux) project at the Woods Hole Oceanographic Institution (WHOI) is a research project, with central foci on air-sea exchanges of heat, moisture, and momentum and their role in global climate variability and change. The OAFlux has distributed global time series of ocean evaporation, air-sea latent and sensible heat fluxes, and flux-related surface meteorological variables from 1958 onward with a near real-time update (<http://oaflux.whoi.edu>). In the past four years, efforts have been devoted to develop a high-resolution (0.25-degree) global daily analysis of ocean-surface vector winds for the satellite period (July 1987 onwards) through synergizing 12 sensors including both scatterometers and passive microwave radiometers. The new 25-year analysis of ocean surface vector wind extends OAFlux existing surface flux data base, making it a site of choice for consistent, quality, multidecadal time series of air-sea heat, moisture, and momentum fluxes.

The technical report series have four parts, aiming to provide a systematic and conceptually organized review of the 12-sensor synergy and to support the public release of the datasets. This is the first part, focusing on the methodology, approaches, and challenging issues in developing the multi-sensor synthesis. The second part will address the approach of error estimation that is developed to address sensitivity of the OAFlux time series to intersensor differences at high winds and heavy rainfall conditions and to quantify the confidence of the synthesis. The report provides an extended description of the methodology on OAFlux multi-sensor synthesis, with major results drawn from a research paper, entitled “A satellite-derived high-resolution ocean-surface vector wind analysis (1987 onward). Part I: Insight on the synergy between scatterometers and microwave radiometers” [*Yu and Jin 2013a*].

The 12 satellite sensors used in the OAFlux synthesis included 2 scatterometers, and 10 passive microwave radiometers. Scatterometers are microwave radar instruments designed to measure near-surface wind velocity (both speed and direction) over the oceans [*Naderi et al. 1991; Figa-Saldana et al. 2002*]; they surpass passive microwave radiometers [*Hollinger et al. 1990; Wentz 1997*] that provide only wind speed measurements but no wind direction information. Passive polarimetric microwave radiometer is a new type of passive microwave sensor that is equipped with an ability of retrieving both ocean wind speed and vector through measuring the complex correlation between vertically and horizontally polarized microwave radiation [*Gaiser et al. 2004*]. The OAFlux wind time series encompasses the entire era of satellite observations of global ocean-surface winds that starts from the first launch of the Special Sensor Microwave/Imager (SSM/I) on the Defense Meteorological Satellite Program (DMSP) in July 1987. Albeit a wind speed only sensor, the series of SSM/I instruments that were launched subsequently on different platforms, together with the follow-on Special Sensor Microwave Imager/Sounder (SSMIS) sensors that have been in operation since 2005, constitutes a continuous data record of global wind speed for 25 years and continuing. During this period, several scatterometers were launched. The SeaWinds scatterometer onboard the National Aeronautics and Space Administration (NASA) QuikSCAT mission between 1999 and 2009 has provided the longest time series of vector wind measurements with research quality [*Risien and Chelton 2008; Vogelzang et al. 2011*], serving as a vital data source for research and operational applications in a wide range of weather/climate phenomena including tropical cyclones and El Niño. Presently, three scatterometers have demonstrated significant capability of filling the void left by the loss of QuikSCAT. Two are from the Advanced scatterometer (ASCAT) system by the European Meteorological Satellite Organization (EUMESAT) [*Figa-Saldaña et al., 2002*],

with the first launched in March 2007 aboard the operational meteorological satellite MetOP-A and the second launched in September 2012 aboard the MetOP-B satellite. The third scatterometer is the operational satellite OceanSat-2 [Padia, 2010] launched in September 2009 by the Indian Space Research Organization (ISRO). Presently, ASCAT from MetOP-A is used in the OAFlux synthesis. Including the two additional scatterometers will enhance the scatterometer coverage, sampling frequency, and the observation continuity. The OAFlux project is a research project, and efforts are being made to continue exploring new scatterometers to ensure continuity and quality of the vector wind time series with given available resources.

This report addresses the methodology, approaches, and challenging technical issues in developing the OAFlux multi-sensor synthesis. Given that scatterometers and microwave radiometers (section 2) measure different electromagnetic properties at the ocean surface, one fundamental issue is to what degree wind retrievals from the two different instruments can be synergized. This report will begin with the rationale that supports the synergy of scatterometers and radiometers (section 3), and then proceed to discuss the methodology and strategy that was developed for the OAFlux objective synthesis (section 4), the challenging issues that were encountered during the synthesis (section 5), and validity of the OAFlux synthesized daily-mean fields with reference to scatterometers and atmospheric reanalyses (section 6). A summary and conclusion is given in section 7.

2. Input satellite sensors

2.1 Type of wind sensors used in the OAFlux synthesis

The 12 sensors in the OAFlux synthesis include six SSMI sensors (F08, F10, F11, F13, F14, and F15), two SSMIS sensors (F16 and F17), AMSRE, WindSat, QuikSCAT, and ASCAT.

The time line for each of the 12 sensors is shown in Figure 1. A summary of the sensor characteristics and accuracy is given below.

SSM/I: The SSM/I sensor is a seven channel passive microwave radiometer operating at four frequencies (19.35, 22.235, 37.0, and 85.5 GHz) and dual-polarization (except at 22.235 GHz which is V-polarization only). SSM/I covers 82% of the earth surface between 87°36'S and 87°36'N in 24 hours with footprint ranging from 13 km to 69 km, depending on the channel and location along the 1394 km scanning swath [*Hollinger et al.*, 1990; *Wentz* 1997]. SSMI was first launched onboard the DMSP F8 satellite on 19 June 1987 and subsequent SSMIs have been launched on later DMSP satellites (F10, F11, F13, F14, and F15). Wind speed retrievals are available under both clear and cloud conditions but can be contaminated when cloud/rain liquid water values exceed 18 mg cm^{-2} . *Mears et al.* [2001] showed that mean difference between SSMI winds and buoy winds is less than 0.5 m s^{-1} and the standard deviation of the difference is around 1.3 m s^{-1} .

SSMIS: The SSMIS sensor is the next-generation SSMI. With 24 discrete frequencies from 19 to 183 GHz and a swath width of 1700 km, the conically scanning SSMIS offers improved atmospheric temperature soundings, water vapor soundings, and surface observations. SSMIS represents the most complex operational satellite passive microwave imager/sounding sensor ever flown. The instrument became operational in November 2005 onboard the DMSP F16, with one additional onboard F17 in March 2008. Buoy comparisons based on the observations between November 2003 and July 2005 [*Kunkee et al.*, 2008] showed that the performance of SSMIS F16 was very similar to SSMI F13, F14, and F15, with the mean difference less than 0.2 ms^{-1} for all sensors and a standard deviation between 1.7 and 1.9 ms^{-1} .

Here, the shorter study period (21 months) is perhaps the reason that the standard deviations of SSMIs are slightly higher than those mentioned above from *Mears et al.* [2001].

AMSR-E: The AMSR-E sensor was launched on 4 May 2002 aboard the NASA's Aqua spacecraft. It is a *dual polarized* microwave radiometer with six frequency channels at 6.9, 10.6, 18.7, 23.8, 36.5 and 89 GHz. The low frequency channels (6.9 and 10.6 GHz) penetrate deeper and are more sensitive to sea surface temperature and wind but less sensitive to the atmosphere [*Meissner and Wentz* 2002]. The SST and wind speed algorithms are essentially the same, except that the SST algorithm uses all five AMSR-E lower-frequency channels, while the wind algorithm does not use the 6.9 GHz channels because of the lack of improvement. The improved sensitivity of AMSRE to surface wind and temperature improves the accuracy of wind speed retrievals when compared to SSM/I [*Meissner and Wentz* 2002]. Additionally, AMSR-E scans conically across a 1445-km swath, providing nearly 100% daily coverage for the ocean areas poleward of 45° north and south latitudes and more than 80% daily coverage for the mid-latitudes. Comparison of the collocated AMSR-E and TAO buoy winds yielded a mean difference of 0.3 ms^{-1} and the standard deviation of the difference of 1.1 ms^{-1} [*Konda et al.* 2009].

WindSat: The WindSat onboard the Air Force Coriolis mission on 6 January 2003 is the first space-based polarimetric microwave radiometer designed to measure the ocean surface wind vector [*Gaiser et al.* 2004]. The five channels at 6.8, 10.7, 18.7, 23.8 GHz, and 37.0 GHz are similar to those of the AMSR-E sensor except that WindSat does not have an 89 GHz channel. The frequencies at 10.7, 18.7, and 23.8 GHz are fully polarized and these polarization signals contain a small dependence on wind direction that can be used for wind vector retrievals [*Yueh et al.* 1995; *Laursen and Skou* 2001]. WindSat observations are comparable to scatterometers for

wind speeds at and above 8 ms^{-1} , but wind direction uncertainty can be substantial for wind speed [Wentz *et al.* 2005; Quilfen *et al.* 2007]. Our input data quality control performed before the OAFflux synthesis [Yu and Jin 2012] indicated that WindSat wind direction retrievals are not consistent with scatterometer direction retrievals and differ considerably from in situ buoy measurements. Thus, OAFflux included only WindSat wind speed retrievals but no direction retrievals.

QuikSCAT: The SeaWinds on the NASA's QuikSCAT mission is an active radar scatterometer transmitting microwave pulses at a frequency of 13.4 GHz (Ku-band). Wind speed and direction at 10 m above the surface of the water are derived from the backscatter energy. The instrument has an unprecedented large swath width of 1800 km, covering 93% of the global oceans in 24 hours, and providing a continuous, high quality ocean vector wind data record for more than 10 years from 19 June 1999 to 23 November 2009. Accuracy of QuikSCAT wind measurements is estimated at more or less 1 ms^{-1} for wind speed and 20° for wind direction based on concurrent buoy and ship measurements [Ebuchi *et al.* 2002; Bourassa *et al.* 2003; Vogelzang *et al.* 2011]. It is worth noting that the accuracy quoted here cannot be met in the nadir part of the swath, where the QuikSCAT geometry is less favorable for both speed and direction measurement and for rain screening [e.g. Portabella and Stoffelen 2001].

ASCAT: ASCAT is a C-band (5.255 GHz) dual fan-beam radar scatterometer onboard the EUMETSAT METOP-A satellite on 19 October 2006. MetOp-A is followed by MetOp-B, which was launched in November 2012, and MetOp-C, which is planned in 2017. This series altogether will provide for at least 15 years of operational scatterometer datasets. The ASCAT fan-beam antennae cover two 550-km wide swaths separated by a 720 km wide gap, providing about 60-65% of the coverage of QuikSCAT because the latter had a single continuous 1800 km

wide swath (no nadir gap). The C-band has a major advantage over the Ku-band in that it is much less affected by direct rain effects and can operate in all-weather conditions. Hence, ASCAT has a unique position of providing reliable observations for the most intense and often cloud-covered wind phenomena.

2.2 Processing and quality-check satellite retrievals

The OAFlux synthesis obtained the 25km Level 2 ASCAT wind vectors from the Physical Oceanography Distributed Active Archive center at the Jet Propulsion Laboratory (<http://podaac.jpl.nasa.gov/>), with the source data at both 12.5 km and 25 km sampling resolution [Verspeek *et al.* 2010] located at the Ocean and Sea Ice Satellite Application Facility web pages (OSI SAF) at the Royal Netherlands Meteorological Institute (KNMI) (www.knmi.nl/scatterometer) [ASCAT Wind Product User Manual, 2012]. The datasets of other sensors at 25-km resolution were downloaded from the Remote Sensing Systems (RSS) company (<http://www.ssmi.com/>). In particular, the SSMI products were from version 6, SSMIS from version 7, AMSRE from version 7, WindSat from version 7, and QuikSCAT from version 4. All the downloaded input wind products were calibrated as equivalent neutral stability winds at a height of 10 m.

Rain affects all wind retrievals from all microwave sensors [Weissman *et al.* 2012]. Rain contaminated retrievals were discarded by using rain flags embedded in the products. Radiometers provide no wind retrievals whenever rain presents. The land-sea mask in the OAFlux wind analysis was originally taken from the 0.25° daily Optimum Interpolation (OI) SST analysis by Reynolds *et al.* [2007]. The mask was further adjusted by expanding the coastlines 50 km into the sea for pre-QuikSCAT years and 25 km into the sea for the QuikSCAT

period. Sea ice margins change on daily basis so that daily sea-ice mask was constructed based on the sea-ice concentration provided by the National Snow and Ice Data Center. Any grid point that has sea-ice concentration above 50% is treated as ice grid.

Satellite sensors can be drifted by several factors, with the sources being physical, geometrical, mechanical, mapping, environmental, random, etc. Some of the drifts may be long-term, some short-term, and some both. Satellite orbital drift, sensor degradation, sensor offsets, and signal interference are the common causes of long-term drifts and often lead to bias in the retrievals. For the SSMI sensor series, the instruments were originally designed for weather and environmental applications and their long-term performance stability has not been thoroughly assessed to date. Therefore, different SSMI sensors have to be carefully calibrated to a reference satellite or a stable reference system before used in the synthesis. For the OAFlux project, an in situ validation database consisting of 126 buoy time series *Yu and Jin* [2012] was established to provide a ground truth for checking potential drifts in input data sets (Figure 2). Among the 126 buoy time series in use, 67 are from the Tropical Atmosphere Ocean/TRIangle Trans-Ocean buoy Network (TAO/TRITON) in the tropical Pacific Ocean [*McPhaden et al.*, 1998], 21 from the Pilot Research Moored Array in the Atlantic (PIRATA) [*Bourlès et al.*, 2008], and 18 from the Research Moored Array for Africa-Asian-Australian Monsoon Analysis and Prediction (RAMA) in the tropical Indian Ocean [*McPhaden et al.*, 2009]. The three tropical array networks constitute a total of 106 buoys. The 20 other buoys include the moored buoys at the Kuroshio Extension Observatory (KEO) [*Cronin et al.*, 2008] and the ocean climate station Papa in the Gulf of Alaska [*Kamphaus et al.* 2008], and 18 archived/active moored buoys deployed by WHOI at flux reference sites and the sites selected for targeted field programs [*Colbo and Weller* 2009]. The list of buoy locations can be found in *Yu and Jin* [2012].

Buoy winds are usually sampled at 3–4 m height and transmitted at every 5- or 60-minute interval depending upon the design of instruments, while satellite winds are the equivalent neutral winds at the height of 10m. For consistency, daily buoy winds (wind speed, direction, zonal and meridional components) were constructed from scalar averaging of the measurements at available sample frequency over each day. Quality control flags in the data files were applied to reject bad or low-quality measurements. These daily buoy winds were then adjusted to the 10 m neutral winds following *Tang and Liu* [1996].

Mean drifts were identified in some sensors and were truncated from the time series to prevent their potential bias effect on the synthesis. The mean drifts in input wind retrievals are illustrated in Figure 3a, showing, for instance, that SSMI F14 and F15 drifted away around 2005-06 and ASCAT was low biased before 2008. The periods of abnormality in these sensors were truncated and the actual data periods used in the synthesis are shown in Figure 3b.

3. Rationale supporting the synergy between scatterometers and radiometers

3.1 A theoretical perspective

A scatterometer measures the microwave backscatter from the wind-roughened sea surface. A radiometer measures the sea-surface microwave emissions that are sensitive to surface roughness created by wind forcing. The two instruments use different electromagnetic properties to retrieve ocean-surface winds, but they have one feature in common. Scattering and emission from the sea surface both describe the electromagnetic wave diffraction from surface short-scale waves (i.e. gravity-capillary and capillary surface waves with wavelengths in the range of a millimeter to several centimeters) that generate surface roughness.

The so-called two-scale scattering approximation [*Phillips* 1957] is the most widely accepted theoretical model of the scattering and emission from the ocean surface [*Wentz*, 1975; *Brown* 1979; *Plant* 1986; *Donelan and Pierson* 1987; *Yueh et al.* 1994; *Lemaire et al.* 1999]. The basic idea of the two-scale model is to divide the surface wave spectrum into two parts: one corresponds to the Kirchhoff regime for the large-scale component that can be approximated as specular reflection, and the other corresponds to the Bragg regime for the small-scale component with modulation from tilts of large-scale waves. For satellite scatterometry, the primary mechanism for backscattering radar pulses is the Bragg resonance, and the secondary mechanism is the longer wave modification of local incidence angle through tilting the Bragg resonance surface roughness. For satellite radiometry, the two modes of waves together with sea foam – the latter becomes important for wind speeds above 8ms^{-1} – are three important types of roughness scales that contribute to ocean surface emissivity [*Meissner and Wentz* 2012]. These roughness contributions to the surface emissivity can be approximated as integral functions of the product of electromagnetic weighting functions and the surface roughness spectrum [*Yueh et al.*, 1994; *Wentz* 1997]. The weighting functions have resonance peaks when surface wave length scale is comparable to the electromagnetic wavelength. In this regard, both active and passive remote sensing problems depend on the roughness properties of small-scale wave components in the vicinity of Bragg resonance [*Donelan and Pierson* 1987; *Yueh et al.* 1994; 1995].

In analyzing coincident measurements with a 37-GHz polarimetric radiometer and a 10-GHz scatterometer from an aircraft field experiment conducted in 1995, *Weissman et al.* [2002] showed that both scatterometer and radiometer in study respond to short sea surface waves of very similar wavelengths and have similar sensitivity to wind speed (or friction velocity) and direction. Their analysis provided supporting evidence that the azimuthal signatures of the two

instruments are from the same geophysical process: the angular dependence of short waves on the ocean surface and the tilting of the local incidence angle by the longer waves. On the other hand, their analysis also revealed that the two instruments have different dependences on the incidence angle with respect to the longer wave tilting effect. While the intensity of the brightness temperature increases with the increasing incidence angle [Yueh *et al.*, 1995], the strength of scatterometer sigma-0 decreases with the increasing incidence angle [Schroeder *et al.* 1985; Wentz and Smith 1999]. The opposite dependence of the two sensors on the incidence angle becomes more apparent at low incidence angles and high wind speeds [Plant *et al.* 1999; Freilich and Vanhoff 2003]. SSMI measurements are made at a nominal incidence angle of 51°, while scatterometers measurements are obtained from a range of incidence angles.

3.2 Evidence from active and passive sensor retrievals

The compatibility between active and passive remote sensing of ocean-surface winds are examined by using wind retrievals from 2 scatterometers (QuikSCAT and ASCAT) and three radiometers (SSMIS F17, AMSRE, and WindSAT). Figure 4 shows the scatter plots of daily collocations of QuikSCAT with respect to each of the other four sensors for the year 2009. In these plots, collocated wind speeds were binned into 1 ms⁻¹ bins and plotted with QuikSCAT on x axis and each of the four other sensors on the y axis for wind speeds ranging from 0 to 35 ms⁻¹. Rain contaminated retrievals have all been discarded. Figure 4a-d display the relationships between sensors in low (< 5 ms⁻¹), moderate (5-15 ms⁻¹), and high wind speed (>15 ms⁻¹) ranges for rain-free conditions. As shown in Figure 4a, ASCAT agrees well with QuikSCAT up to 15 ms⁻¹. For wind speed greater than 15 ms⁻¹, ASCAT is systematically weaker than QuikSCAT, with magnitude of bias increasing with increasing wind speed (Figure 4a). For instance, ASCAT

is about 5 ms^{-1} lower than QuikSCAT when the latter is at 20 ms^{-1} and about 8 ms^{-1} lower when the latter is at 30 ms^{-1} . The inter-scatterometer difference at high winds is consistent with existing literature that ASCAT is biased low when winds are strong [e.g. *Bentamy et al. 2011; Yu and Jin 2012*].

Compared to ASCAT, the three passive microwave radiometers show a near-linear relationship with QuikSCAT. SSMIS F17 has the best consistency with QuikSCAT for the entire range of wind speeds under examination. WindSat and AMSRE agree well with QuikSCAT, albeit the two radiometers tend to be slightly higher than QuikSCAT for extremely high wind speeds ($>20 \text{ ms}^{-1}$). Given the discussion in the above section, radiometer and scatterometer have similar sensitivity to wind speed and direction because they respond to similar short-scale wavelengths. The good agreement between all sensors at low and moderate wind speed range appears to support the theoretical rationale. On the other hand, the two instruments are also different because they have opposite dependence on the incidence angle at high wind speeds. The stronger radiometer wind retrievals when wind speeds exceed 20 ms^{-1} seem to be explainable from the theoretical point of view.

3.3 Global wind distribution in low, moderate, and high wind categories

Given the inter-scatterometer differences at high winds, questions thus raised are how often and where high winds occur, as answers to these questions will help to assess the degree of potential impacts of inter-sensor differences at high winds on the multi-sensor synthesis. To examine these questions, we first identify the regions that are most frequented by high winds. Figure 5a shows the total high-wind days for an average year constructed over the 25-year period (1988-2012) from the available eight SSMI and SSMIS sensors. Obviously, most high wind

events occur at latitudes of westerly winds between 30-60° in both hemispheres. The maximum occurrence is associated with the southern hemisphere westerly wind belt, where the total number of high wind days exceeds 40 days per year in most areas and up to 65 days in the Indian Ocean sector. The second maximum occurrence is in the subpolar North Atlantic Ocean basin, where on average there are about 40-50 days of high-wind events each year. Almost all the high winds occur during the respective hemisphere's fall/winter seasons.

We then investigate the percentage of global distribution of high winds by grouping the wind at 0.25-degree grids into the three wind speed categories: low, moderate, and high winds. The SSMI/SSMIS wind speed observations during the 1988-2012 period were used for computation. Figure 5b shows that, on an annual basis, high winds account only for 2.2% over the global field, while low winds and moderate winds are about 20.2% and 77.6%, respectively. The evidence shows that 98% of the global daily wind fields are subject to low and moderate winds, with high winds contributing to a mere 2%.

Low and moderate winds are the range of wind retrievals that scatterometers and radiometers have the best agreement and best quality. Thus, the theoretical and practical aspects for integrating radiometers and scatterometers are mutually supporting. The compatibility between all sensors for wind speeds below 15 ms⁻¹ and the 98% dominance of the low and moderate winds on the global scale establishes a solid base that wind retrievals from the two different types of sensors can be integrated.

4. Methodology and strategy of synthesis

4.1 Methodology

The methodology of the OAFlux objective synthesis is based on the theory of the least-variance linear statistical estimation [Daley 1991; Talagrand 1997]. It allows the formulation of a least-squares estimator (the so-called cost function) to include not only data from different sources but also a priori information that one wishes to impose to constrain the solution. The approach has been used to produce the OAFlux analysis of global ocean evaporation, latent and sensible heat fluxes [Yu, 2007; Yu and Weller, 2007; Yu et al., 2008]. In developing the OAFlux ocean surface vector wind analysis, a major technical challenge was to derive the directional information that is consistent with the SSM/I wind speed retrievals for the pre-QuikSCAT years when there were no scatterometer datasets in input data sources (Figure 1). Our strategy was to utilize the surface vector wind fields from atmospheric reanalysis as the first guess for zonal (u) and meridional (v) wind components, and adjust u and v iteratively by imposing two types of constraints. One is that (i) the analyzed wind speed $w = \sqrt{u^2 + v^2}$ should be as close as possible to satellite wind speed retrievals in a least-squares sense, and the other is that (ii) the solution of (u, v) should satisfy a set of kinematic constraints such as vorticity and divergence conservations [Hoffman 1984; Legler et al. 1989; Stoffelen and Anderson 1997; Vogelzang et al. 2009; Atlas et al. 1996; 2011].

Under these considerations, the cost function formulated for the OAFlux synthesis, F , can be expressed as follows:

$$\begin{aligned}
 F = & \underbrace{\frac{1}{2}(\vec{V}_a - \vec{V}_b)^T R_b (\vec{V}_a - \vec{V}_b)}_{\text{(I)}} + \underbrace{\frac{1}{2}(\vec{V}_a - \vec{V}_o)^T R_o (\vec{V}_a - \vec{V}_o)}_{\text{(II)}} + \underbrace{\frac{1}{2}(w_a - w_o)^T S_o (w_a - w_o)}_{\text{(III)}} + \dots \\
 & + \underbrace{\gamma(\nabla \times \vec{V}_a - \nabla \times \vec{V}_b)^2}_{\text{(IV)}} + \underbrace{\lambda(\nabla \cdot \vec{V}_a - \nabla \cdot \vec{V}_b)^2}_{\text{(V)}}
 \end{aligned} \tag{1}$$

where $\vec{V} = (u, v)$ is wind vector with zonal and meridional wind components denoted as u and v , respectively, and $w = \sqrt{u^2 + v^2}$ is wind speed. The superscript “ T ” denotes transpose. There are three subscripts: “ a ” denotes an estimate, “ b ” the background information, and “ o ” satellite observations. Two atmospheric surface wind reanalyses are used as the background data, including the European Centre for Medium-Range Weather Forecasts Re-Analysis (ERA) interim project [Dee *et al.* 2011] and the Climate Forecast System Reanalysis (CFSR) from the National Centers for Environmental Prediction (NCEP) [Saha *et al.*, 2010]. To be consistent with the format of satellite wind retrievals, the reanalyzed winds were adjusted to the height of 10 m equivalent neutral winds following Tang and Liu [1996]. Among the 12 satellite sensors in use, QuikSCAT and ASCAT have observations of zonal and meridional wind components while all others are radiometers providing only wind speed observations. WindSat is used as a radiometer in the OAFflux synthesis, since its wind direction retrievals have large uncertainty when compared to buoy measurements and with QuikSCAT [Yu and Jin 2012]. The matrices R_b , R_o , and S_o are weighting matrices that, theoretically, are inversely proportional to the respective error covariance matrices of the background wind vector fields (\vec{V}_b), satellite wind vector observations (\vec{V}_o), and satellite wind speed observations (w_o).

There are five terms on the right hand side of the cost function (1). The first three terms (I)-(III) are data constraints that represent a least-squares fitting of the analyzed zonal wind, meridional wind, and wind speed to input background and satellite data sets. ERAinterim and CFSR supply the background information that is needed for two occasions: (i) initialization of wind direction when there are no scatterometer measurements prior to 1999, and (ii) gap-filling missing values in satellite observations. The fourth and fifth terms (IV)-(V) are weak constraints based on vorticity and divergence of ERAinterim and CFSR, and the contribution of these

kinematic terms to the minimization process is set to be small by prescribing the scaling γ and λ respectively. The minimization process seeks an optimal estimate of daily wind field that satisfies the data constraints (i.e., terms (I)-(III) in Eq.(1)) within the specified weight matrices for the given sets of weak constraints (i.e., terms (IV)-(V)). A conjugate-gradient method was used for the optimization and the process was similar to the one applied in constructing OAFflux latent and sensible heat fluxes [Yu *et al.* 2008].

4.2 Weight assignment

The weight associated with each term in the cost function (1) is inversely proportional to the error covariance matrix of input data field. If an input dataset has large uncertainty, the contribution of input data to the cost function is small, and vice versa. In other words, the weights determine the goodness of fit between analyzed variable fields and input data fields. However, none of input data sources described in section 2 provide error estimates for satellite wind speed/direction retrievals. The lack of error information for input datasets limits our ability to prescribe "true" weights for the terms in the cost function (1). In light of the situation, we resorted to in situ air-sea buoys to guide the weight assignments based on the buoy evaluation of input satellite datasets. It is worth noting that buoy winds are the independent validation reference for the OAFflux analysis; they are not included in the cost formulation (1).

For simplicity, we assume that the weights are constant and the cost function (1) can be simplified as follows:

$$\begin{aligned}
F = & \underbrace{\frac{1}{2} \sum_{i=1}^I \alpha_i (u_a - u_i)^2}_{\text{(I)}} + \underbrace{\frac{1}{2} \sum_{i=1}^I \alpha_i (v_a - v_i)^2}_{\text{(II)}} + \underbrace{\frac{1}{2} \sum_{j=1}^J \beta_j (w_a - w_j)^2}_{\text{(III)}} + \dots \\
& + \underbrace{\gamma (\nabla \times \vec{V}_a - \nabla \times \vec{V}_b)^2}_{\text{(IV)}} + \underbrace{\lambda (\nabla \cdot \vec{V}_a - \nabla \cdot \vec{V}_b)^2}_{\text{(V)}}
\end{aligned} \tag{2}$$

where α_i represents the weight assignment for zonal and meridional wind components, with the subscript $i = 1, \dots, I$ indicating the respective input satellite (i.e., QuikSCAT and ASCAT) plus background (i.e., ERAinterim and CFSR) data sets for wind components. The weight assignment for wind speed term is denoted by β_j , with the subscript $j = 1, \dots, J$ indicating the respective input satellite wind speed data sets (e.g., SSMI F08, F10, F11, F13, F15, SSMIS F16, F17, AMSRE, WindSat, QuikSCAT, and ASCAT). The weights, β_j , associated with wind speed constraint (term (III)) were set to be 1. For the period when only one scatterometer is available, the weight associated with the scatterometer derived u and v constraints (terms (I) and (II)) was taken as the sum of the number of available wind speed data sets. For instance, there were six wind speed datasets (SSMI F13, SSMIS F16 and F17, AMSRE, WindSat, and QuikSCAT) for the synthesis in 2008 but only one u and v dataset from QuikSCAT. We set $\alpha_2 = 6$ in order to balance the contribution from wind speed constraints. The weights of the ERAinterim u and v terms, α_i , were assigned to be 0.8, and the weights of the kinematic constraints for vorticity and divergence, γ and λ , were fixed at 0.5. All the weights were constant, due to the lack of in situ measurements to define the latitude dependence of errors. As will be shown in Part II of the study [Yu and Jin 2013b], the sensitivity of the optimal solution to weight assignments can be used to formulate the uncertainty estimation of the synthesis.

5. Challenging issues for the multi-sensor synthesis

5.1 Selection of resolution

The 25-km resolution is a nominal resolution used in processing all satellite wind retrievals and is the spatial resolution taken by the OAFlux synthesis. However, the selection of the temporal resolution is a trade-off between the optimality of the solution of Eq.(1) and data coverage from available sensors. The solution of Eq.(1) is optimal only when there are sufficient observations that random errors in data can be reduced and the error variance can be minimal. During the 25-year analysis period, the number of available sensors varies with time (Fig.1). The time series starts with one sensor in July 1987, followed by two- or three-sensor constellation over most of the 1990s, and expanding up to a maximum of 7-sensor constellation in the mid-2000s. Figure 6a shows the global coverage for two temporal resolutions, six hourly and daily, based on the sensor combinations that occurred during the analysis period. All rain flagged wind retrievals were excluded in the computation. Removal of rain contamination reduces the total number of wind retrievals by 2-10% depending on the sensor type. Figure 6a suggested that, if a six-hourly resolution is used, the percentage of global coverage changes from 27%, when only one SSMI is available, to a maximum of 79%, when QuikSCAT and four radiometers (AMSRE and 3 SSMI sensors) are available. On the other hand, if a daily resolution is chosen, the minimum coverage is 75% for the first few years when there is only one SSMI sensor and is near global (~98%) during the QuikSCAT period (1999 – 2009). After November 2009, a combination of ASCAT with SSMIS provides up to 94% global coverage. The difference in daily coverage between ASCAT and QuikSCAT is due to ASCAT configuration. The 1100 km ASCAT coverage consists of two 550 km swaths separated by a 720 km nadir gap for a total width of about 1820 km. This configuration yields an average 70% of daily coverage over the

global ocean. QuikSCAT has a continuous 1800 km wide swath and samples about 93% of the global ocean each day. It should be noted that a full 100% coverage is not likely because of rain. The Ku-band QuikSCAT is sensitive to heavy rains, while passive radiometers have no observations under all rain conditions. The C-band ASCAT is less sensitive to direct rain effects [Portabella *et al.* 2012], but the daily coverage at 70% is not sufficient to cover all the rain areas that radiometers have no observations.

From a least squares perspective, if the number of observations over the global grid points is less than the number of grid points, the minimization problem is underestimated and has infinite solutions (or no unique solution). In this case, one needs to rely on the background dataset (such as the reanalysis) to select a solution, which makes the estimated vector wind fields at the solution lean heavily toward the background information for the regions that have no satellite observations. If the background datasets, such as reanalysis winds, have a coarser spatial resolution and a smoother pattern, they would show up in the estimated wind fields and cause an uneven distributed spatial structure, resulting in finer-scale spatial variability in the regions covered by satellites and a smooth structure in the regions of no satellite data. Hence, we selected daily resolution for OAFlux product to ensure a maximum global coverage and to provide optimal conditions for the optimality of the solution.

5.2 Data Gap Filling

Missing data over the open ocean are caused mainly by two factors: interswath gaps between ascending and descending passes and the elimination of rain-contaminated wind vector cells. In some cases, the shutdown of satellite instrument when an anomaly is detected on the spacecraft can cause the loss of satellite observations for an extended period of time. Impact of

instrument shutdown is felt more sharply before 1997 (Figure 6b) when there were only 1-2 sensors available. Wind fields from numerical weather prediction models are resorted upon when satellite observations are lacking, which is a practice commonly used. For instance, the removal of directional ambiguity in scatterometer measurements was initialized by the operational 10-m NCEP nowcast analysis in producing the standard QuikSCAT wind products [e.g. *Chelton and Freilich, 2005*]. The six-hourly cross-calibrated multiplatform (CCMP) ocean surface wind product [*Atlas et al. 2011*] applied the 40-year ECMWF Re-Analysis (ERA40) and operational analysis to fill in sampling gaps and to provide the first guess. For the OAFlux synthesis, the model winds used as the background information were the 6-hourly 0.7° gridded ERA-interim winds [*Dee et al. 2011*].

Atmospheric reanalyzed winds are not satellite winds although satellite winds are assimilated in the models. To use ERAinterim winds for gap filling, the differences between the ERAinterim and satellite need to be mitigated. The approach we implemented is described in Figs. 7a-f using the synthesis on 1 January 1990 as an example. There was one passive microwave radiometer (i.e. SSMI F08) available at that time and so the effect of the gap filling on the final solution can be seen more clearly. Each SSMI sensor has two time files per day (ascending and descending passes), marked by Coordinated Universal Time (UTC) in tenths of hours. Each time file represents the corresponding time of the swath sample used to interpolate the given grid cell for either ascending or descending orbits. OAFlux synthesis was conducted on daily mean basis, but gap filling was performed for each satellite pass using the 6-hourly ERA-interim at the nearest time. By doing so, short-term variability (such as isolated short-lived storms, fast-moving synoptic system, diurnal rainfall variability, etc) can be better represented instead of being smoothed out by daily means.

Figures 7a-b display the coverage of global wind speed field from the respective ascending and descending passes. The gaps between overpass swaths together with the loss of observations under rain lead to missing data over a considerable spatial extent. The first step of gap filling was to match the ERA-interim six-hour intervals (Fig. 7e-f) with the nearest observing time associated with the ascending and descending passes (Figs. 7c-d). The next step was to use the selected reanalysis six-hour products to fill in SSMI gaps. Satellite winds are known to be higher than winds from global reanalysis models both in the mean and for extreme cases [Brown 2002; Yu and Jin 2012]. An adjustment was made to ERAinterim using a three-day mean satellite field for wind speed fields only. Zonal and meridional wind components have directions and the gap filling approach cannot be applied. The final synthesized wind speed field is shown in Fig.7g.

5.3 Sensitivity of daily-mean field to heavy rain associated with strong storms

The most challenging situation for the multi-sensor synthesis is the high-wind, heavy-rain storm system. Passive microwave radiometers have no observations under rain conditions, while the C-band ASCAT and the Ku-band QuikSCAT have different responses to rain, causing persistent inter-scatterometer difference in high winds over the overlapping areas [Weissman *et al.* 2012]. One case analysis is presented in Figures 8-9, in which satellite wind observations of Hurricane Bill on 22 August 2009 from four sensors are examined. On that day, the storm was located in the northwest Atlantic, and satellite wind observations of the system include wind speed and direction retrievals from ASCAT and QuikSCAT and also wind speed retrievals from AMSRE and SSMIS F17. WindSat, SSMI F13, and SSMIS F17 were also available at that time and were used in producing the OAFflux synthesis. But for simplicity, the three sensors were not

presented here, as the three radiometers have similar characteristics to those of AMSRE and SSMI F17. Their role in the synthesis is to increase the number of samplings over the rain-free regions which helps to optimize the solution, but the impact on reconstructing the near-surface wind pattern associated with rain is limited because they provide no observations when rain presents.

Figures 8a-d show the daily coverage of the Atlantic region of interest, [10-60°N, 85-20°W], produced by summing up the ascending and descending passes for each of the four sensors. All retrievals that were flagged by rain were removed. Evidently, the ASCAT's two swaths of 550-km widths with a 720 km wide separation leave large areas between swaths unsampled. Nevertheless, the C-band sensor has a clear advantage of being less susceptible to rain and hence more capable of capturing the storm's near-surface wind field if the storm's location happens to fall within the orbit passes (Figure 8a). On the other hand, rain has a larger effect on attenuating and scattering the radar energy at Ku-band (13.4 GHz) [*Sobieski et al. 1999; Draper and Long 2004*], so that QuikSCAT cannot "see" through heavy rain. As is seen from Figure 8b, a sizable portion of high winds near the storm center is smeared after rain contaminated wind vector cells (WVCs) were removed from QuikSCAT retrievals. The impact of eliminating rain-contaminated QuikSCAT WVCs is seen more clearly from the near-surface wind convergence field ($\partial u/\partial x + \partial v/\partial y$) of the storm (Figs. 9a-b, which are the convergence fields in the boxed area in Figs. 8a-b). The storm's eye and the bands of intense surface convection that spiral around the storm's center are visible in ASCAT, but are distorted significantly in QuikSCAT. Anomalous convergence/divergence lines along the edges of the swaths are shown in both fields, which can attribute largely to the changes of surface wind synoptic variability between the time lapse of the ascending and descending passes. The two passes represent two

time discrete snapshots of satellite observations of surface winds. In case of fast moving weather system, it seems that more sensors (or passes) are needed to better represent variability of the weather system and hence better daily mean.

The OAFflux multi-sensor synthesis is sensitive to the inter-scatterometer differences associated with heavy-rain storms. To demonstrate the effect, two synthesis experiments were conducted. In Experiment I, the synthesis was based on ASCAT and SSMIS F17 and AMSRE, while in Experiment II, the synthesis was based on QuikSCAT and the same two radiometers. In both experiments, missing data in wind speed fields were filled in with mean-adjusted ERA-interim surface wind speeds (Figs.7a-f). The wind speed fields from the two experiments are shown in Figs.10a-b. The two experiments produced very similar pattern and similar magnitude over the broad regional scale except for the storm center, where the inter-scatterometer differences cause the storm's high wind pattern to vary considerably with the experiment. The storm center is more elongated in the QuikSCAT experiment (Exp II) while more rounded in the ASCAT experiment (Exp I).

Depicting the storm center's high winds challenges not only satellite observations but also atmospheric reanalyses. The difficulty for obtaining a consistent pattern of the storm's near-surface wind structure is illustrated in Figs. 10c-d, in which daily-mean wind speed fields from CFSR and ERA-interim are displayed. The two reanalyses, albeit smooth, have a regional pattern in good agreement with the two sensitivity experiments. However, the shape and magnitude of the high winds around the center of the storm differ substantially. Both reanalyses assimilated QuikSCAT and ERA-interim included also ASCAT. The lack of consistency between reanalyses underlines the models' deficiencies in capturing synoptic variability of near-surface wind.

5.4 Sensitivity of daily-mean field to high winds and rain on the global scale

A global view of the inter-scatterometer differences and their effects on the OAFlux multi-sensor synthesis on 22 August 2009 is examined in Figs. 11-12. On that day, ASCAT alone provides 65% of the global coverage and missing data are due primarily to the gaps between swaths (Fig. 11a). QuikSCAT covers 85% of the global oceans, and missing data are attributable to both interswath gaps and heavy rain contamination (Fig. 11b). The two radiometers, AMSRE and SSMIS 17 have a global coverage of 68% and 74% respectively, and the effect of rain on causing data gaps is particularly pronounced along the tropical rain belts of the Intertropical Convergence Zone (ITCZ) and the South Pacific Convergence Zone (SPCZ).

The global wind speed fields produced by the two sensitivity experiments, Exp I (Fig.12a) and Exp II (Fig. 12b), have good agreement in spatial details over the global scale but differ in synoptic scales associated with propagating weather events. Exp II that used QuikSCAT produced stronger high winds for storms. This is seen not only in the Northwest Atlantic where Hurricane Bill was located (Fig.10a) but also more pungently in the southern midlatitudes between 30-60°S where three intense storms were swirling around, with one located southwest of Australia and the other two in the south Atlantic sector. The wind-speed difference field between ASCAT and QuikSCAT retrievals (Fig.12c) shows that, despite an incomplete global picture, the difference anomalies exceed 3ms^{-1} are located primarily in the mid latitude storm track regions (30-60 degree north and south). The wind-speed difference plot between OAFlux EXP I and EXP II (Fig.12d) shows that the synthesis has reduced considerably the difference anomalies between the two sensors, and the magnitude of differences larger than 1ms^{-1} occurs mostly at locations of high wind speeds induced by passing storms. This suggests that the inclusion of radiometers in the multi-sensor synthesis can accommodate most of the differences

in the scatterometers, except for high winds. Clearly, the two sensitivity experiments demonstrate that high winds and rain are two leading sources of uncertainty in synthesizing wind retrievals from different types of sensors.

5.5 Sensitivity of the OAFlux time series to high winds

Using SSMI and SSMIS sensors over the 25-year analysis period, we showed in Figs. 5a-b indicate that the low and moderate winds account for nearly 98% of daily global wind field while high winds account for a mere 2% and occur predominantly at midlatitudes between 30-60 degrees north and south. The distribution of the high-wind days constructed from OAFlux time series (Fig.13a) suggests that OAFlux high wind frequency is consistent with SSMI and SSMIS sensors.

Low and moderate winds dictate the annual-mean time series of globally averaged wind speeds. Figure 13b shows the three sets of time series of global-mean averages constructed with and without high winds. The first one was for the OAFlux synthesized wind speeds in full range, the second one for setting wind speeds greater than 15 ms^{-1} to 15 ms^{-1} , and the third one for setting wind speeds greater than 20 ms^{-1} to 20 ms^{-1} . If limiting wind speeds to no more than 15 ms^{-1} , the time series that sets maximum wind speed to 15 ms^{-1} has a reduced magnitude (by 0.04 ms^{-1} or 0.5%) compared to the original dataset but has no noted changes in annual-mean variability. By comparison, the time series that sets maximum wind speed to 20 ms^{-1} shows no major difference from the original dataset in either magnitude or yearly variations.

6. Validity of the OAFlux synthesized fields

The meaning of the OAFlux synthesized daily mean is different from that of the scatterometer-based daily mean. OAFlux constructs the daily mean field from multiple sensors, with the number of passes (descending+ascending) ranging from 2 to 14 per day during the analysis period. On the other hand, the daily mean field of a satellite sensor is the summation of two passes, i.e., ascending and descending passes, for each day. Here the daily mean fields from OAFlux are compared with scatterometers to elucidate the differences between the two and daily wind fields from atmospheric reanalyses are also included for value-added analysis.

6.1 Daily mean from scatterometers

Satellite passes are more like “snapshot” views of global fields. The representation of daily mean is affected not only by the global coverage but also by sampling noise (random error) in the retrievals. From a statistical point of view, the errors have larger effect on wind derivatives (e.g. wind convergence, vorticity, and wind stress curl) than on winds, because the accuracy of wind derivatives usually reflects the error magnitude in winds. The global fields of near-surface wind convergence/divergence fields from ASCAT and QuikSCAT on 22 August 2009 is presented in Figures 14a-b. Portion of these fields in the northwest of the Atlantic has been used for a close-up of the scatterometer’s capability to depict the near-surface circulation associated with Hurricane Bill (Figs.9a-b). The global pattern is compounded severely by the noises in scatterometer retrievals. Detailed structures are not easily identifiable, although one could judge from the color scales (e.g. positive denotes convergence) that there should be an enhanced level of surface convergence in regions associated with the Inter-Tropical Convergence Zone (ITCZ), the South Pacific Convergence Zone (SPCZ), and extratropical storms. To uncover useful features in the scatterometer observations, a spatial filter (1-2-1) was applied twice to smooth out some noises (Figs. 14c-d). After the smoothing, one feature that can be better appreciated is the

convergence/divergence in small-scale filamentary structures that are organized in regions of surface frontal zones, including the ITCZ and SPCZ in the tropics and the mid-latitude synoptic weather systems. The filamentary pattern is better seen in QuikSCAT field, as it is less interrupted by the diamond-shaped missing data gaps compared to ASCAT.

6.2 Daily mean from the OAFlux synthesis

The surface convergence/divergence on 22 August 2009 constructed from OAFlux (Fig. 15a) resembles closely to that from twice-filtered QuikSCAT (Fig.14d) but with less grid-point noises. The OAFlux filamentary structure is more acutely defined compared to QuikSCAT and ASCAT, perhaps the spatial filter (1-2-1) that was twice applied to scatterometer fields has also smoothed out some signals. A noted convergence structure in Fig. 15a is the ITCZ in the tropical Pacific around 10-15°N latitudes, where the system meanders from the coast of Panama to near the dateline, with segments of strong convection (denoted by large positive values) filaments embedded along two discrete bands. However, when examining the monthly-mean convergence field in August 2009 (Fig. 15b), the filamentary form of convergence is barely visible. Instead, the ITCZ latitudes (10-15°N) in the Pacific and Atlantic are the location of the maximum convergence over the global oceans, and the equatorial band (0-5°N) lying south of the ITCZ is the location of the maximum divergence. The difference between daily and monthly means suggests that the monthly mean reflects the ensemble average of daily mean. The frequent occurrence of discrete, fine-scale convergence/divergence filaments along the ITCZ latitudes produces a broad zonal band of convergence maximum. It should be noted that convection and convergence are different concepts, and the actual convection usually does not collocate with the convergence zone. Convergence describes the near-surface air converging on the center of low

surface pressure, while convection describes the vertical motions. The convection cells are usually found on the north side of the convergence zone with their southern boundaries close to the convergence line [*Bony et al.* 1997; *Lau et al.* 1997].

6.3 Daily-mean differences between OAFlux and atmospheric reanalyses

OAFlux synthesis is not independent of ERAinterim and CFSR, as the latter two provide the background information for filling in missing data gaps in wind speed and for initializing the vector components when scatterometers are not available. Since both reanalyses assimilate scatterometers, their surface fields should be constrained by scatterometers to some degree. However, they differ from QuikSCAT. The near-surface convergence/divergence fields from the two reanalyses are shown in Figs. 16a-b, respectively. Similar filamentary structures are evidenced, but the magnitude is weaker and spatial details are smoother. Furthermore, ERAinterim is dictated mostly by convergence (positive) filaments. The divergence (negative) filaments that are so ubiquitous in OAFlux (Fig. 15a) and scatterometers (Figs. 14c-d) are hardly seen in ERAinterim. CFSR has both convergence and divergence filaments. But the problem of CFSR is the spurious oscillations of small-scale convergence and divergence at low and mid latitudes, which appear to be the artifacts of the Gibbs ripples [*Navarra et al.*, 1994].

Two other reanalyses are also examined, which are the latest reanalyses by the NASA's modern-era retrospective analysis for research and applications (MERRA; *Rienecker et al.* [2011]), and the NCEP/NCAR reanalysis (hereafter NCEP1). Neither MERRA nor NCEP1 was included in the OAFlux synthesis. Similar to ERAinterim (Fig.16a), MERRA (Fig. 16c) has predominantly convergence filaments and limited divergence filaments. NCEP1 (Fig. 16d) has no filamentary structures in sight, due perhaps to its coarse resolution (i.e. 1.875°). All

reanalyses assimilate scatterometers, but their wind derivatives deviate substantially from each other. The differences in surface wind convergence/divergence pattern and magnitude suggest that errors in surface wind products are still large and affect the fidelity of wind derivatives.

6.4 OAFlux and atmospheric reanalyses before QuikSCAT

The daily-mean fields examined in Figs. 14-16 fall at a time when both QuikSCAT and ASCAT were available. For the years before September 1999, there is no influence of scatterometer on OAFlux. It would thus be interesting to see whether the small-scale filaments still exist in OAFlux. For this purpose, the daily-mean field on 25 August 1998 was chosen, as on that day there was a category-3 storm, Hurricane Bonnie, heading toward north and northwest in the North Atlantic. The daily-mean convergence/divergence fields from the four products: OAFlux, ERAinterim, MERRA, and CFSR, are shown in Figs. 17a-d, respectively. Interestingly, the comparison yields the similar results to those found in Figs. 15-16. All products have captured the synoptic convergence/divergence filaments but differ in the spatial details of the filamentary structure. OAFlux shows the filaments in the form of convergence-divergence couplets, which differs from the three reanalyses that show the convergence-dominant filaments. CFSR has a comparably stronger divergence component among the three reanalyses, but the Gibbs ripples in the low and mid latitudes cause some contamination to the global field. The difference between the satellite-based synthesis and atmospheric reanalyses indicates that much still needs to be learned on the structural and physics of air-mass convergence in the mid latitudes along meso-scale fronts. Nevertheless, the comparison indicates that the divergence filaments in OAFlux are not scatterometer dependent, and they are presented in both pre-1999 and post-1999.

Differences between OAFlux and the three latest reanalyses are substantial during severe storm events for the pre-QuikSCAT period. The surface convergence/divergence fields in the Northwest Atlantic area are enlarged to close-up the near-surface fields associated with Hurricane Bonnie (Figs. 18a-d). The four products are similar in depicting the northwestward orientation of the storm but are different in the detailed structure of the storm center. The three reanalyses show a slanted blob of high surface convergence with slight variation in magnitude. By contrast, OAFlux shows a much richer detail, featuring the storm's eye (i.e. the small area of divergence in the middle of convergence), the eyewall (i.e, the intense convergence surrounding the eye), and the disintegrated divergence clusters to the northeast of the storm. Apparently, the OAFlux synthesis has captured better the fine details of surface convergence/ divergence associated with synoptic storm system for the pre-QuikSCAT period.

7. Summary

A high-resolution global analysis of daily ocean-surface vector winds that covers the entire satellite wind observing period, from the first launch of SSMI in July 1987 to the present, was developed by the Objectively Analyzed air-sea Heat Fluxes (OAFlux) project. The 25-year vector wind analysis was a synergy of 12 satellite sensors that included 2 scatterometers (QuikSCAT and ASCAT), and 10 passive microwave radiometers (AMSRE, 6 SSMI series, 2 SSMIS series, and the passive polarimetric microwave radiometer from WindSat (only wind speed retrievals were used)).

An insight on synergizing scatterometers and radiometers is presented in this study. Four issues were addressed, including the rationale that supports the synergy of scatterometers and radiometers, the methodology and strategy that was developed for the OAFlux objective

synthesis, the challenging issues that were encountered during the synthesis, and the validity of the OAFlux synthesized daily-mean fields with reference to scatterometers and atmospheric reanalyses.

It is found that synergizing scatterometer and radiometers is supported theoretically and practically. Scattering and emission from the sea surface both describe the electromagnetic wave diffraction from surface short-scale waves that generate surface roughness in the vicinity of the Bragg resonance. The two sensors have a similar angular dependence of short waves on the ocean surface, but differ in their dependence on the incidence angle with respect to the longer wave tilting effect, particularly at high wind speeds ($>15\text{ms}^{-1}$). Our analysis showed that, on an annual basis, high winds account only for a mere 2% over the global field, and low winds and moderate winds for about 20% and 78%, respectively. Our analysis also showed that scatterometers and radiometers have high accuracy and consistency in the low and moderate wind speed range, but bifurcate in the high wind speed range. That 98% of the global surface wind fields are low and moderate winds and are best retrieved by both scatterometers and radiometers establishes the background for developing the methodology of synthesis.

The methodology of the OAFlux objective synthesis is based on the theory of the least-variance linear statistical estimation, which leads to the formulation of a least-squares estimator (the so-called cost function) to include not only data from different sources but also a priori information to constrain the solution. The cost function of the OAFlux synthesis has two sets of constraints. One is that the analyzed zonal (u) and meridional (v) winds, and wind speed $w=\text{sqrt}(u^2+v^2)$ should be as close as possible to satellite retrievals and input background information in a least-squares sense, and the other is that the solution of (u,v) should satisfy a set of kinematic constraints such as vorticity and divergence conservations. ERAinterim and CFSR

provided the background information that is needed for two occasions: (i) initialization of wind direction when there are no scatterometer measurements prior to 1999, and (ii) gap-filling of missing values in satellite observations. The minimization process seeks an optimal estimate of daily wind field that satisfies the data constraints within the specified weight matrices.

The issues need to be carefully considered before synergizing scatterometers and radiometers include quality check of input satellite datasets, error statistics of input datasets, selection of temporal resolution, and filling in data gaps. In situ validation database consisting of 120+ buoy time series measurements has played an important role in the OAFflux synthesis. These buoy measurements were not used for synthesis; rather, they remained as an independent validation reference in the synthesis that led to the identification of the period of SSM/I sensors that has mean drifts and of bias in WindSat wind direction retrievals. The in situ database also helped to diagnose the error statistics in input datasets and determine the weight assignments for each dataset included in the least-squares estimator.

The selection of temporal resolution is based on the maximum global coverage that the satellite sensors can provide throughout the entire satellite era. When the global coverage over the entire 25 years is considered, daily resolution is a sensible choice based on the requirement of the least-squares principle. Specifically, if observations have errors, the number of observations over the global grid points needs to be greater than the number of grid points to ensure that the minimization is an overestimated problem. This allows the random errors in data to cancel each other out so that the solution thus obtained has a minimum variance. However, even with a daily resolution, a complete 100% global daily coverage over the ice-free oceans is not obtained, because of the sensor's sensitivity to rain conditions. When one sensor is considered, 5-10% global ocean grids are affected by rain. When multiple sensors are combined, about 2% of global

grids are still influenced by rain. The use of the background reanalysis data to fill in the gaps is needed literally on every day. The OAFflux performed gap filling for each satellite pass by using the 6-hourly mean-adjusted ERAinterim wind speed at the nearest time to better represent short-term variability in data gap regions.

The most challenging issue during the OAFflux multi-sensor synthesis is the construction of the near-surface circulation associated with synoptic weather storms due mainly to three factors. One is the lack of radiometer retrievals when rain presents. The second is the rain contamination in QuikSCAT. The elimination of rain-flagged QuikSCAT wind vector cells leaves data voids that cannot be easily filled in by the background ERAinterim. The third reason is the scatterometer difference at high wind conditions, as ASCAT high winds are persistently lower than QuikSCAT high winds. The two experiments that compared the respective influence of ASCAT and QuikSCAT on radiometer based synthesis showed that the large-scale pattern and magnitude are barely affected by the inter-scatterometer differences but the surface wind fields associated with synoptic weather systems are scatterometer-dependent. Therefore, the estimates of the 2% global winds that are influenced by rain and high-wind conditions have a degree of uncertainty.

Wind derivatives are a measure of the errors of wind products. It is found that the structure of daily-mean surface wind convergence/divergence field varies with product. Scatterometer daily surface convergence fields are too noisy to discern any meaningful spatial patterns; but after spatial filtering, meso-scale filaments of surface convergence/divergence and couplets are evidenced in regions associated with the ITCZ, SPCZ, and mid-latitude surface fronts. OAFflux daily mean shows refined spatial details of these filaments and couplets. On the other hand, reanalyzed fields are different, not only because of the smoother structure but most

importantly, because of the overwhelming dominance of convergence filaments with limited divergence activity. Among all the reanalysis products, CFSR has a better depiction of the divergence filaments but the Gibbs ripples contaminate the global pattern.

In summary, this part one study provided an insight on the theory of the synergy between scatterometers and radiometers and the practical use of the least-variance linear statistical estimation in producing a consistent time series of ocean vector wind from multiple satellite sensors on multiple platforms. The improved depiction of mesoscale filamentary structure associated with fronts demonstrates the advantage and benefits of OAFlux in applications to mesoscale air-sea interaction, which demonstrates also that objective synthesis is a viable platform for merging the advantages of sensors from different platforms. As global climate has been and continues to change and the wind is an essential variable in all air-sea interaction processes, the scientific values of a continuous and consistent surface vector wind time series of 25 years are yet to be evaluated. In part two of the study [*Yu and Jin, 2013b*], the confidence and sensitivity of the OAFlux time series to uncertainties in satellite retrievals will be addressed.

Acknowledgements

The project is sponsored by the NASA Ocean Vector Wind Science Team (OVWST) activities under grant NNA10AO86G. We thank the support and technical inputs from the international OVWST members during the 5-year development of the OAFlux wind synthesis products. The OAFlux datasets are freely available from the project website at <http://oaflux.who.edu/>. The satellite wind products of SSMI, SSMIS AMSRE, and QuikSCAT were downloaded from Remote Sensing Systems at <http://www.ssmi.com/>, and ASCAT datasets from NASA JPL PO.DAAC at <http://podaac.jpl.nasa.gov>. The original ASCAT datasets are hosted by KNMI at <http://www.knmi.nl/scatterometer>. ERA-interim, CFSR, and NCEP reanalyses were downloaded from the NCAR Research Data Archive at <http://rda.ucar.edu>, and MERRA was downloaded from the Global Modeling and Assimilation Office (GMAO) and the GES DISC at <ftp://goldsmr2.sci.gsfc.nasa.gov>.

References

- ASCAT Wind Product User Manual (2013). Version 1.13. May 2013. Ocean and Sea Ice SAF. 23pp. Available from http://www.knmi.nl/scatterometer/publications/pdf/ASCAT_Product_Manual.pdf.
- Atlas, R., R.N. Hoffman, S.C. Bloom, J.C. Jusem, and J. Ardizzone, 1996: A multiyear global surface wind velocity dataset using SSM/I wind observations. *Bull. Amer. Meteor. Soc.*, **77**, 869-882.
- Atlas, R., R. N. Hoffman, J. Ardizzone, S. M. Leidner, J. C. Jusem, D. K. Smith, and D. Gombos (2011). A cross-calibrated, multiplatform ocean surface wind velocity product for meteorological and oceanographic applications. *Bull. Amer. Meteor. Soc.*, **92**, 157-174. doi: 10.1175/2010BAMS2946.1.
- Attema, E. (1991). The active microwave instrument onboard the ERS-1 satellite. *Proc. IEEE*, **79**(6), 791-799.
- Bentamy, A., Y. Quilfen, P. Flament, (2002). Scatterometer wind fields: A new release over the decade 1991-2001. *Canadian J. Remote Sensing*, **28**(3), 431-449.
- Bentamy, A., D. Croizé -Fillon, and C. Perigaud (2008). Characterization of ASCAT measurements based on buoy and QuikSCAT wind vector observations. *Ocean Sci.*, **4**, 265-274.
- Bentamy, A., S. A. Grodsky, J. A. Carton, D. Croizé-Fillon, and B. Chapron (2012). Matching ASCAT and QuikSCAT winds. *J. Geophys. Res.* **117**, C02011, doi:10.1029/2011JC007479.
- Bourassa, M. A., D. M. Legler, J. J. O'Brien, and S. R. Smith (2003). SeaWinds validation with research vessels, *J. Geophys. Res.*, **108**, C2, 3019.

- Bony, S., K.-M. Lau, and Y. C. Sud (1997). Sea surface temperature and large-scale circulation influences on tropical greenhouse effect and cloud radiative forcing. *J. Climate*, **10**, 2055-2076.
- Bourlès, B., R. Lumpkin, M. J. McPhaden, F. Hernandez, P. Nobre, E. Campos, L. Yu, S. Planton, A. J. Busalacchi, A. D. Moura, J. Servain, and J. Trotte (2008). The PIRATA Program: History, accomplishments, and future directions. *Bull. Amer. Meteorol. Soc.*, **89**, 1111-1125, doi.org/10.1175/2008BAMS2462.1.
- Brown, R. A. (2002). Scaling effects in remote sensing applications and the case of organized large eddies. *Can. J. Remote Sens.*, **28**, 340-345.
- Brown, G. S. (1979). Estimation of surface wind speeds using satellite-borne measurements at normal incidence. *J. Geophys. Res.*, **84**, 3974-3978.
- Chelton, D. B. and M. H. Freilich (2005). Scatterometer-based assessment of 10-m wind analyses from the operational ECMWF and NCEP numerical weather prediction models. *Mon. Wea. Rev.*, **133**, 409–429. doi: <http://dx.doi.org/10.1175/MWR-2861.1>.
- Chin, T. M., R. F. Milliff, and W. G. Large, 1998: Basin-scale, high wavenumber, sea surface wind fields from a multiresolution analysis of scatterometer data. *J. Atmos. Oceanic Technol.*, **15**, 741–763.
- Colbo, K., and R. A. Weller (2009). The accuracy of the IMET sensor package in the subtropics. *J. Atmos. Oceanic Technol.*, **26**(9), 1867-1890.
- Cronin, M. F., C. Meinig, C. L. Sabine, H. Ichikawa, and H. Tomita (2008). Surface mooring network in the Kuroshio Extension. *IEEE Systems Special Issue on GEOSS*, **2**(3), 424-430.
- Daley, R. (1991). *Atmospheric Data Analysis*. Cambridge University Press, 457pp.

- Dee, D. P., and co-authors. (2011). The ERA-Interim reanalysis: configuration and performance of the data assimilation system. *Q. J. R. Meteorol. Soc.*, **137**, 553-597. doi: 10.1002/qj.828.
- DeMoss, J. D., and K. P. Bowman (2007). Changes in TRMM rainfall due to the orbit boost estimated from buoy rain gauge data. *J. Atmos. Oceanic Technol.*, **24**, 1598-1607. doi: <http://dx.doi.org/10.1175/JTECH2082.1>.
- Donelan, M. A., and W. J. Pierson (1987). Radar scattering and equilibrium ranges in wind-generated waves with application to scatterometry. *J. Geophys. Res.*, **92**, 4971-5029.
- Draper, D. W., and D. G. Long (2004). Simultaneous wind and rain retrieval using SeaWinds data. *IEEE Trans. Geosci. Remote Sens.*, **42**, 1411-1423.
- Ebuchi, N., H. C. Graber, and M. J. Caruso (2002). Evaluation of wind vectors observed by QuikSCAT/SeaWinds using ocean buoy data, *J. Atmos. Ocean. Technol.*, **19**, 2049-2069.
- Figa-Saldaña, J., J. J. W. Wilson, E. Attema, R. Gelsthorpe, M. R. Drinkwater, and A. Stoffelen (2002). The advanced scatterometer (ASCAT) on the meteorological operational (MetOp) platform: A follow on for European wind scatterometers. *Can. J. Remote Sens.*, **28**(3), 404-412.
- Freilich, M. H. and R. S. Dunbar (1999), The accuracy of the NSCAT-1 vector winds: Comparisons with NDBC buoys. *J. Geophys. Res.*, **104**, 11,231-11,246.
- Freilich, M. H., and R. S. Dunbar (1999). The accuracy of the NSCAT-1 vector winds: Comparisons with NDBC buoys. *J. Geophys. Res.*, **104**, 11,231-11,246.
- Gaiser, P. W., and co-authors. (2004). The WindSat spaceborne polarimetric microwave radiometer: Sensor description and early orbit performance. *IEEE Trans. Geosci. Remote Sens.*, **42**, 2347-2361.

- Hoffman, R. N. (1984). SASS wind ambiguity removal by direct minimization. Part II: Use of smoothness and dynamical constraints. *Mon. Wea. Rev.*, **112**, 1829-1852.
- Hoffman, R. N., S. M. Leidner, J. M. Henderson, R. Atlas, J. V. Ardizzone, and S. C. Bloom (2003). A two-dimensional variational analysis method for NSCAT ambiguity removal: Methodology, sensitivity, and tuning. *J. Atmos. Oceanic Technol.*, **20**, 585-605.
- Hollinger, J.P., J. L. Peirce, and G. A. Poe (1990). SSM/I instrument evaluation. *IEEE Trans. Geosci. Remote Sens.*, **28**(5), 781-790.
- Kamphaus, R., M. Cronin, C. Sabine, S. Emerson, C. Meinig, and M. Robert (2008). New surface mooring at Station Papa monitors climate. *PICES Press*, **16**(2), 26-27.
- Kelly, K. A., S. Dickinson, M. J. McPhaden, and G. C. Johnson (2001), Ocean currents evident in satellite wind data, *Geophys. Res. Lett.*, **28**(12), 2469–2472, doi:10.1029/2000GL012610.
- Konda, M., H. Ichikawa, and H. Tomita (2009). Wind speed and latent heat flux retrieved by simultaneous observation of multiple geophysical parameters by AMSR-E. *J. Remote Sens. Soc. Japan*, **29**, 191-198.
- Kunkee, D. B., G. A. Poe, D. J. Boucher, S. D. Swadley, Y. Hong, J. E. Wessel, and E. A. Uliana (2008). Design and Evaluation of the First Special Sensor Microwave Imager/Sounder. *IEEE Trans. Geosci. Remote Sens.*, **46**(4), 863–883.
- Lemaire D, P. Sobieski, and A. Guissard (1999). Full-range sea surface spectrum in nonfully developed state for scattering calculations. *IEEE Trans. Geosci. Remote Sens.*, **37**, 1038-1051.
- Lau, K.-M., H.-T. Wu, and S. Bony (1997). The role of large-scale atmospheric circulation in the relationship between tropical convection and sea surface temperature. *J. Climate*, **10**, 381-392.

- Laursen, B., and N. Skou (2001). Wind direction over the ocean determined by an airborne, imaging, polarimetric radiometer system. *IEEE Trans. Geosci. Remote Sens.*, **39**(7), 1547-1555.
- Legler, D. M., I. M. Navon, and J. J. O'Brien (1989). Objective analysis of pseudo-stress over the Indian Ocean using a direct minimization approach. *Mon. Wea. Rev.*, **117**, 709-720.
- McPhaden, M. J., and co-authors (1998). The Tropical Ocean-Global Atmosphere observing system: A decade of progress. *J. Geophys. Res.*, **103**(C7), 14,169-14, 240, doi:10.1029/97JC02906.
- McPhaden, M. J., G. Meyers, K. Ando, Y. Masumoto, V. S. N. Murty, M. Ravichandran, F. Syamsudin, J. Vialard, L. Yu, and W. Yu (2009). RAMA: The Research Moored Array for African-Asian-Australian Monsoon Analysis and Prediction. *Bull. Ameri. Meteor. Soc.*, **90**, 459-480.
- Mears, C. A., D. K. Smith, and F. J. Wentz (2001). Comparison of SSM/I and buoy-measured wind speeds from 1987- 1997. *J. Geophys. Res.*, **106** (C6), 11719-11729.
- Meissner, T., and F. J. Wentz (2002). An updated analysis of the ocean surface wind direction signal in passive microwave brightness temperatures. *IEEE Trans. Geosci. Remote Sens.*, **40** (6), 1230-1240.
- Meissner, T., and F. J. Wentz (2012). The emissivity of the ocean surface between 6 and 90 GHz over a large range of wind speeds and Earth incidence angles. *IEEE Trans. Geosci. Remote Sens.*, **50** (8), 3004-3026.
- Milliff, R. F., J. Morzel, D. B. Chelton, and M. H. Freilich (2004), Wind stress curl and wind stress divergence biases from rain effects on QSCAT surface wind retrievals. *J. Atmos. Ocean. Tech.*, **21**, 1216-1231.

- Naderi, F., M. H. Freilich, and D. G. Long (1991). Spaceborne Radar Measurement of Wind Velocity over the Ocean —An Overview of the NSCAT System. *Proc. IEEE*, **79**(6), 850-866.
- Navarra A., W. F. Stern, and K. Miyakoda, (1994). Reduction of the Gibbs oscillation in spectral model simulations. *J. Climate*, **8**, 1169-1183.
- Owen, M. P., and D .G. Long (2009). Land Contamination Compensation for QuikSCAT Near-Coastal Wind Retrieval. *IEEE Trans. Geosci. Remote Sens.* doi:10.1109/TGRS.2008.2005633, 47(3), 839-850.
- Padia, K. (2010). Oceansat-2 Scatterometer algorithms for sigma-0, processing and products format, Version 1.1, April 2010.
- Phillips, O. M. (1957). On the generation of waves by turbulent wind. *J. Fluid Mech.* **2**(5), 417-445.
- Plant, W. J. (1986). Two-scale model for short wind-generated waves and scatterometry. *J. Geophys. Res.*, **91**, 10,735-10,749.
- Portabella, M., and A. Stoffelen (2001). Rain detection and quality control of seawinds. *J. Atm. Oceanic Technol.*, **18**, 7, 1171-1183.
- Portabella, M., A. Stoffelen, W. Lin, A. Turiel, A. Verhoef, J. Verspeek, and J. Ballabrera-Poy (2012). Rain effects on ASCAT-retrieved winds: toward an improved quality control. *IEEE Trans. Geosci. Remote Sens.*, **50**(7), 2495-2506.
- Quilfen, Y., B. Chapron, T. Elfouhaily, K. Katsaros, and J. Tournadre (1998). Observation of tropical cyclones by high-resolution scatterometry. *J. Geophys. Res.*, **103**(C4), 7767-7786.

- Quilfen Y., B. Chapron, and D. Vandemark (2001). The ERS scatterometer wind measurement accuracy: Evidence of seasonal and regional biases. *J. Atmos. Ocean. Technol.*, **18**, 1684-1697.
- Quilfen, Y., C. Prigent, B. Chapron, A. A. Mouche, and N. Houti (2007). The potential of QuikSCAT and WindSat observations for the estimation of sea surface wind vector under severe weather conditions. *J. Geophys. Res.*, **112**(C9), C09023, doi: 10.1029/2007JC004163.
- Reynolds, R. W., T. M. Smith, C. Liu, D. B. Chelton, K. S. Casey, and M. G. Schlax (2007). Daily high-resolution blended analyses for sea surface temperature. *J. Climate*, **20**, 5473-5496.
- Ricciardulli, L, and F. J. Wentz (2011). Reprocessed QuikSCAT (V04) Wind Vectors With Ku-2011 Geophysical Model Function, Report # 043011. Remote Sensing Systems, Santa Rosa, CA, 8pp.
- Rienecker, M. M., and co-authors (2011). MERRA: NASA's modern-era retrospective analysis for research and applications. *J. Climate*, **24**, 3624-3648. doi: <http://dx.doi.org/10.1175/JCLI-D-11-00015.1>.
- Risien, C. M., and D. B. Chelton (2008). A global climatology of surface wind and wind stress fields from eight years of QuikSCAT scatterometer data. *J. Phys. Oceanogr.*, **38**, 2379-2413.
- Saha, S., and co-authors, (2010). The NCEP climate forecast system reanalysis. *Bull. Amer. Meteor. Soc.*, **91**, 1015-1057. doi: <http://dx.doi.org/10.1175/2010BAMS3001.1>.
- Sobieski, P. W., C. Craeye, and L. F. Bliven (1999). Scatterometric signatures of multivariate drop impacts on fresh and salt water surfaces. *Int. J. Remote Sens.*, **20**, 2149-2166.
- Stiles, B., and S. Yueh (2002). Impact of rain on wind scatterometer data. *IEEE Trans. Geosci. Remote Sens.*, **40**, 1973-1983.

- Stoffelen, A. and D. Anderson, (1997), Ambiguity Removal and Assimilation of Scatterometer Data. *Quarterly J. of the Royal. Meteo. Soc.* **123**, 491-518.
- Tang, W., and W. T. Liu (1996). *Equivalent Neutral Wind*, JPL Publication, 96-17.
- Tournadre, J., and Y. Quilfen (2005). Impact of rain cell on scatterometer data: 2. Correction of Seawinds measured backscatter and wind and rain flagging. *J. Geophys. Res.* **110**, C07023, doi:10.1029/2004JC002766.
- Verspeek, J., A. Verhoef, and A. Stoffelen (2010). ASCAT NWP ocean calibration. KNMI Ocean and Sea Ice SAF Rep., 36 pp. [Available online at http://www.knmi.nl/publications/fulltexts/ascat_nwp_ocean_calibration_1.5_copy1.pdf].
- Vogelzang, J., A. Stoffelen, A. Verhoef, J. de Vries, and H. Bonekamp (2009). Validation of two-dimensional variational ambiguity removal on SeaWinds scatterometer data. *J. Atmos. Oceanic Technol.*, **26**, 1229-1245. doi: <http://dx.doi.org/10.1175/2008JTECHA1232.1>.
- Vogelzang, J., A. Stoffelen, A. Verhoef, and J. Figa-Saldaña (2011). On the quality of high-resolution scatterometer winds. *J. Geophys. Res.*, **116**, C10033, doi:10.1029/2010JC006640.
- Weissman, D. E., W. J. Plant, W. C. Keller, and V. G. Irisov, (2002). Comparison of scatterometer and radiometer wind vector measurements. *J. Atmos. Oceanic Technol.*, **19**, 100-113.
- Weissman, D. E., B. W. Stiles, S. M. Hristova-Veleva, D. G. Long, D. K. Smith, K. A. Hilburn, and W. L. Jones (2012). Challenges to satellite sensors of ocean winds: Addressing precipitation effects. *J. Atmos. Oceanic Technol.*, **29**, 356-374. doi: <http://dx.doi.org/10.1175/JTECH-D-11-00054.1>.
- Wentz, F. J., (1975). A two-scale scattering model for foam-free sea microwave brightness temperatures. *J. Geophys. Res.*, **80**, 3441-3446.

- Wentz F. J. (1997). A well-calibrated ocean algorithm for SSM/I. *J. Geophys. Res.*, **102**, 8703-8718.
- Wentz, F. J., T. Meissner, and D. K. Smith (2005). *Assessment of the WindSat retrievals produced by NRL*. RSS Technical Report 010605, 32pp.
- Wentz, F. J. (2013). SSM/I Version-7 Calibration Report, Report # 011012. Remote Sensing Systems, Santa Rosa, CA, 46pp.
- Yu, L. (2007). Global variations in oceanic evaporation (1958-2005): The role of the changing wind speed. *J. Climate*, **20**, 5376-5390.
- Yu, L., and R. A. Weller (2007). Objectively Analyzed air-sea heat Fluxes (OAFlux) for the global ocean. *Bull. Amer. Meteor. Soc.*, **88**(5), 527-539.
- Yu, L., X. Jin, and R. Weller (2008). Multidecade global flux datasets from the Objectively Analyzed Air-sea Fluxes (OAFlux) project: Latent and sensible heat fluxes, ocean evaporation, and related surface meteorological variables. OAFlux Project Tech. Rep. OA-2008-01, 64pp.
- Yu, L., and X. Jin (2012). Buoy perspective of a high-resolution global ocean vector wind analysis constructed from passive radiometers and active scatterometers (1987-present). *J. Geophys. Res.*, **117**, C11013, doi:10.1029/2012JC008069.
- Yu, L., and X. Jin (2013a). A satellite-derived high-resolution ocean surface vector wind analysis (1987 onwards). Part I. Insight on the synergy between scatterometers and microwave radiometers. Submitted.
- Yu, L., and X. Jin (2013b). A satellite-derived high-resolution ocean surface vector wind analysis (1987 onwards). Part II. Confidence and sensitivity to rain and high winds. Submitted.

Yueh, S. H., R. Kwok, and S. V. Nghiem (1994). Polarimetric scattering and emission properties of targets with reflection symmetry. *Radio Sci.*, **29**, 1409-1420.

Yueh, S. H., W. J. Wilson, F. K. Li, S. Y. Nghiem, and W. B. Ricketts (1995). Polarimetric measurements of the sea surface brightness temperature using an aircraft K-band radiometer. *IEEE Trans. Geosci. Remote Sens.* **33**(1), 85-92.

Yueh, S. H., B. W. Stiles, W.-Y. Tsai, H. Hu, and W. T. Liu (2001). QuikSCAT geophysical model function for tropical cyclones and applications to Hurricane Floyd. *IEEE Trans. Geosci. Remote Sensing*, **39**, 2601-2612.

Figure Captions:

Figure 1. Timeline of the 12 sensors included in the OAFflux synthesis.

Figure 2. Validation data base used in the study. The tropical buoy array (RAMA, TAO/TRITON, and PIRATA) is marked by black squares, WHOI archived buoys in blue squares, WHOI active buoys in red squares, and PEMPL buoys in magenta squares.

Figure 3. (a) The original time series of input data sets. Drifts in SSMI F14 and F15 around 2005-06 are evident and low bias in ASCAT before 2009 is also observed. (b) The actual time series of input datasets used in the OAFflux synthesis after truncating the periods of abnormality.

Figure 4. (a) Percentage of global coverage at two possible temporal resolutions: six hourly versus daily, when different sensor combinations are considered. (b) Daily percentage of the ocean areas covered by input sensors over the 25-year analysis period.

Figure 5. (a) Global distribution of the number of days that wind speeds exceed 15ms^{-1} per year constructed from SSMI and SSMIS sensors during the 25-year (1988-2012) period. (b) Percentage of low (light blue), moderate (yellow), and high (dark blue) winds that constitutes the global wind field.

Figure 6. (a) Percentage of the global daily coverage on six hourly and daily for the sensor combination occurred during the 25-year period. (b) Time series of the percentage of the global daily coverage when all available sensors are combined.

Figure 7. Illustration of the gap filling approach using the date on 1 January 1990 as an example. (a) and (b) are SSMI F08 wind speed fields acquired during the ascending and descending orbit passes, respectively. (c) and (d) show the SSMI observing time in UTC for the respective ascending and descending passes. (e) and (f) are the nearest ERA-interim six-hour intervals

that are used to fill in the gaps in the two SSMI passes. (f) is the daily mean field produced from the OAFlux daily synthesis.

Figure 8. Wind speed retrievals on 22 August 2009, the day when Hurricane Bill moved to the northwest Atlantic. Daily coverage from combining ascending and descending passes is shown for (a) ASCAT, (b) QuikSCAT, (c) AMSRE-E, and (d) SSMIS F17. The square box in (a) and (b) is the region of focus in Figure 7, in which wind convergence ($\partial u/\partial x + \partial v/\partial y$) is examined.

Figure 9. Wind convergence ($\partial u/\partial x + \partial v/\partial y$) constructed from (a) ASCAT and (b) QuikSCAT vector wind retrievals on 22 August 2009. The corresponding wind speed retrievals are shown in the boxed region in Figures 8a-b, respectively.

Figure 10. Daily-mean wind speed on 22 August 2009 from (a) OAFlux experiment I using ASCAT, SSMIS F17, and AMSRE; (b) OAFlux experiment II using QuikSCAT, SSMIS F17, and AMSRE; (c) NCEP1, and (d) ERA-interim. The two OAFlux experiments were to test the effect of inter-scatterometer differences in constructing daily mean surface wind field.

Figure 11. Global daily-mean wind speed field on 22 August 2009 from (a) ASCAT, (b) QuikSCAT, (c) AMSRE, and (d) SSMIS. All fields were constructed from summing up the ascending and descending passes.

Figure 12. Global daily-mean wind speed field on 22 August 2009 from (a) OAFlux experiment I using ASCAT, SSMIS F17, and AMSRE; (b) OAFlux experiment II using QuikSCAT, SSMIS F17, and AMSRE; (c) wind speed differences between ASCAT and QuikSCAT; and (d) wind speed differences between OAFlux two experiments.

Figure 13. (a) Global distribution of the number of days that wind speeds exceed 15ms^{-1} per year constructed from SSMI and SSMIS sensors during the 25-year (1988-2012) period. (b) Three sets of annual-mean time series of globally averaged wind speeds: the full range (black),

setting wind speeds greater than 15ms^{-1} to 15ms^{-1} (blue), and setting wind speeds greater than 20ms^{-1} to 20ms^{-1} (red).

Figure 14. Near-surface wind convergence/divergence on 22 August 2009 constructed from (a) ASCAT retrievals, (b) QuikSCAT retrievals, (c) ASCAT retrievals after twice smoothed using a 1-2-1 spatial filter, and (d) QuikSCAT retrievals after twice smoothed using a 1-2-1 spatial filter. Positive values denote convergence and negative values denote divergence.

Figure 15. Near-surface wind convergence/divergence constructed from OAFlux (a) for daily mean on 22 August 2009, and (b) for monthly mean averaged for August 2009. Positive values denote convergence and negative values denote divergence. Note the change of colorbar scale between the two plots.

Figure 16. Near-surface wind convergence/divergence on 22 August 2009 constructed from (a) ERAinterim, (b) CFSR, (c) MERRA, and (d) NCEP1. Positive values denote convergence and negative values denote divergence.

Figure 17. Near-surface wind convergence/divergence on 25 August 1998 constructed from (a) OAFlux, (b) ERAinterim, (c) CFSR, and (d) MERRA. Positive values denote convergence and negative values denote divergence. There was no scatterometer included in OAFlux.

Figure 18. Near-surface wind convergence/divergence associated with Hurricane Bonnie on 25 August 1998 from (a) OAFlux, (b) ERAinterim, (c) CFSR, and (d) MERRA. Positive values denote convergence and negative values denote divergence.

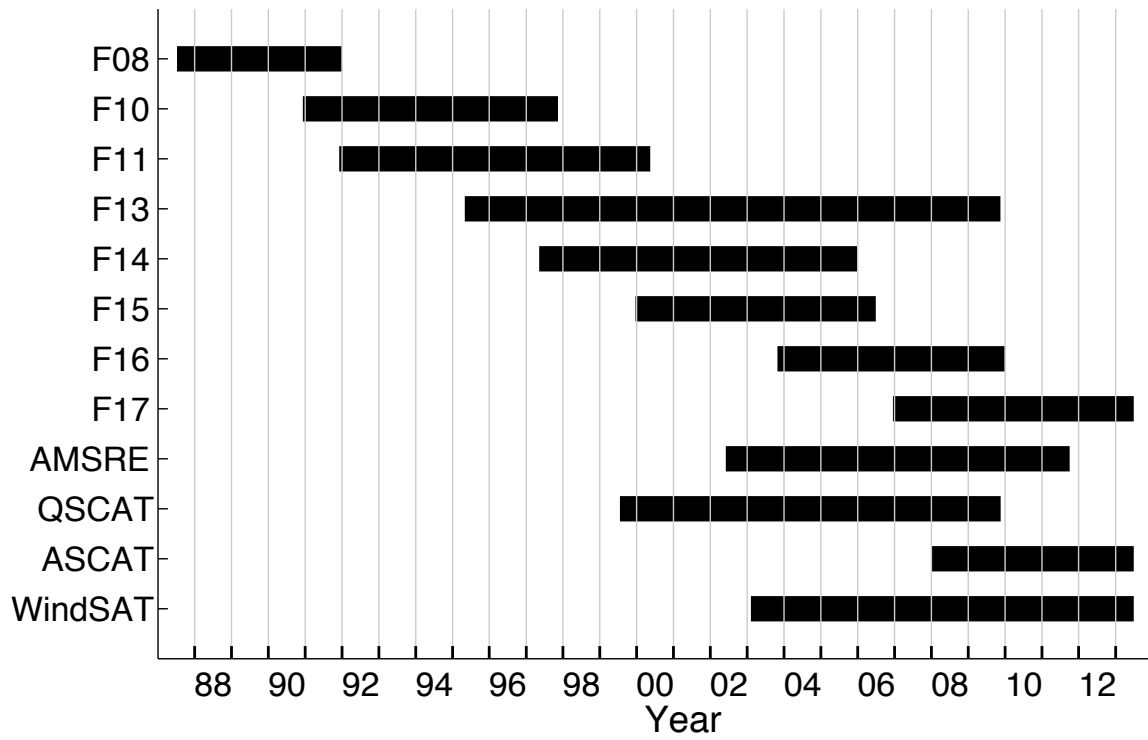


Figure 1. Timeline of the 12 sensors included in the OAFlux synthesis.

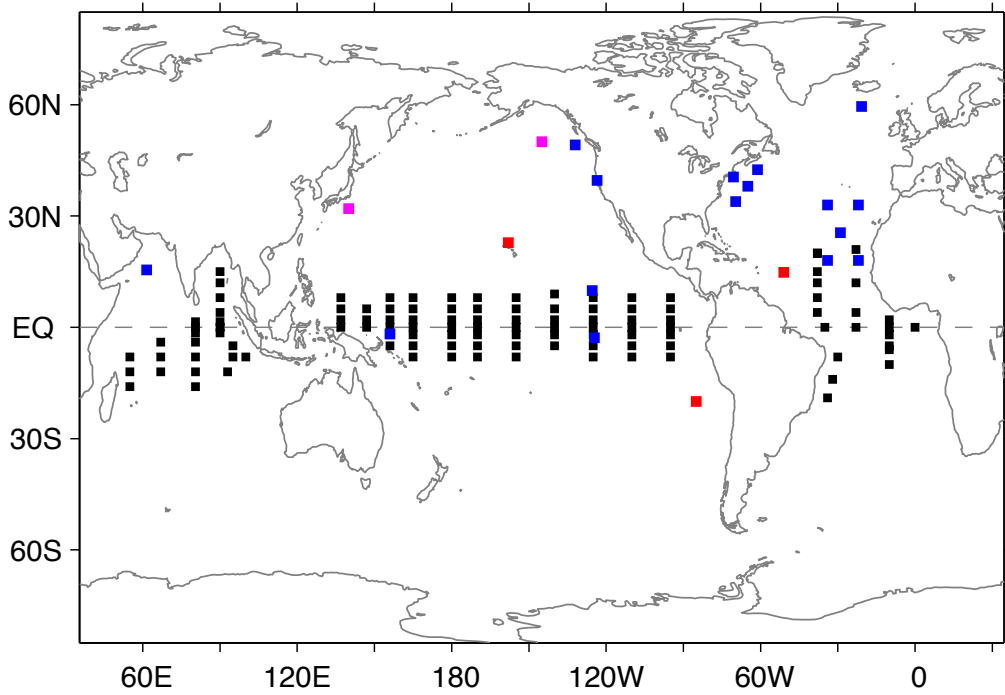


Figure 2. Validation database used in the study. The tropical buoy array (RAMA, TAO/TRITON, and PIRATA) is marked by black squares, WHOI archived buoys in blue squares, WHOI active buoys in red squares, and PEML buoys in magenta squares.

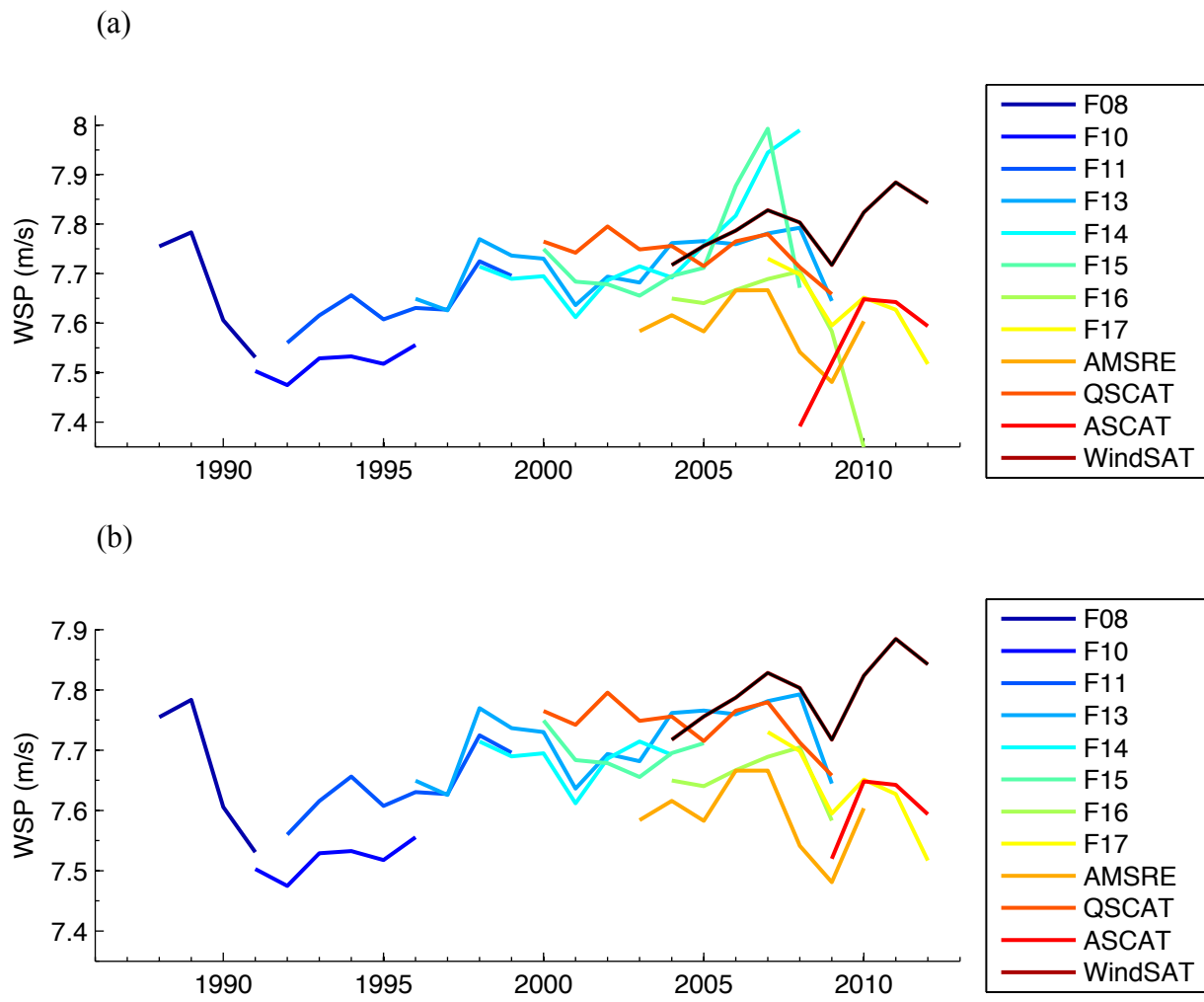


Figure 3. (a) The original time series of input data sets. Drifts in SSMI F14 and F15 around 2005-06 are evident and low bias in ASCAT before 2009 is also observed. (b) The actual time series of input datasets used in the OAF flux synthesis after truncating the periods of abnormality.

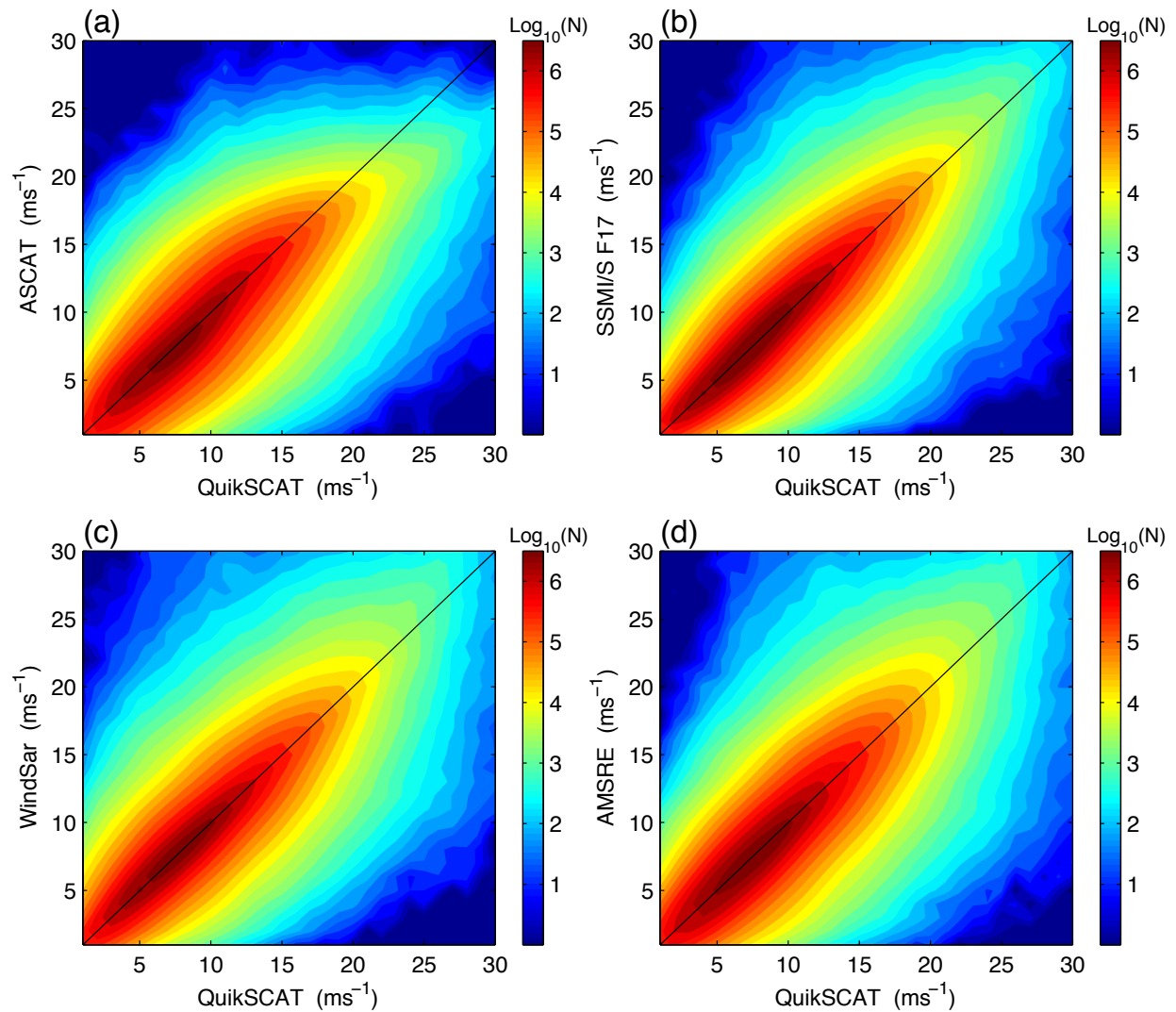


Figure 4. Scatter plots of collocated wind speed pairs in year 2008. (a) ASCAT versus QuikSCAT, (b) SSMIS F17 versus QuikSCAT, (c) WindSat versus QuikSCAT, and (d) AMSRE versus QuikSCAT.

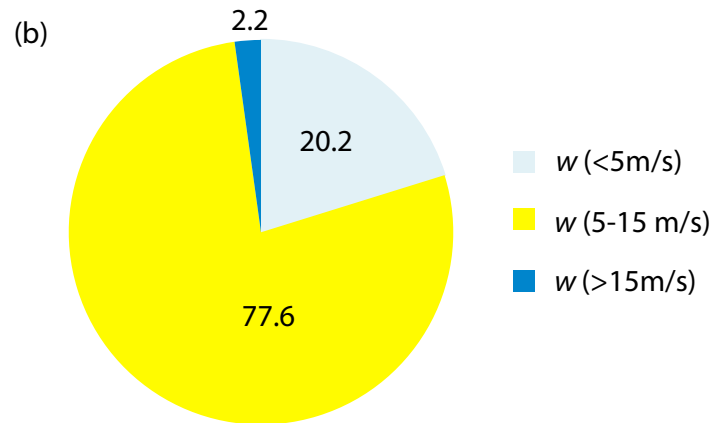
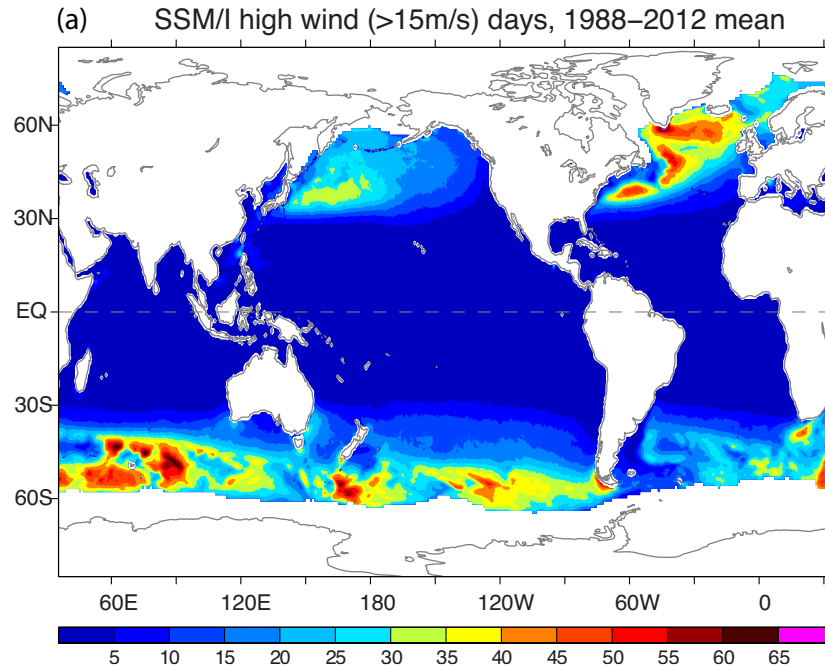
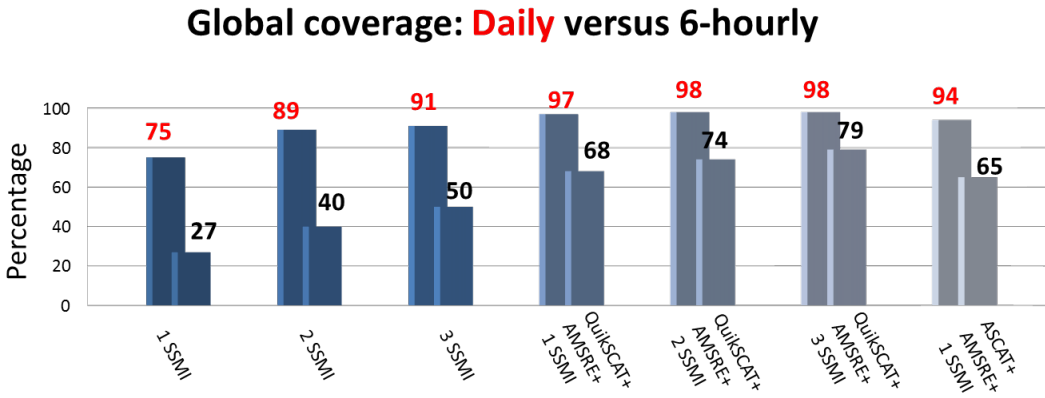


Figure 5. (a) Global distribution of the number of days that wind speeds exceed 15ms^{-1} per year constructed from SSMI and SSMIS sensors during the 25-year (1988-2012) period. (b) Percentage of low (light blue), moderate (yellow), and high (dark blue) winds that constitutes the global wind field.

(a)



(b)

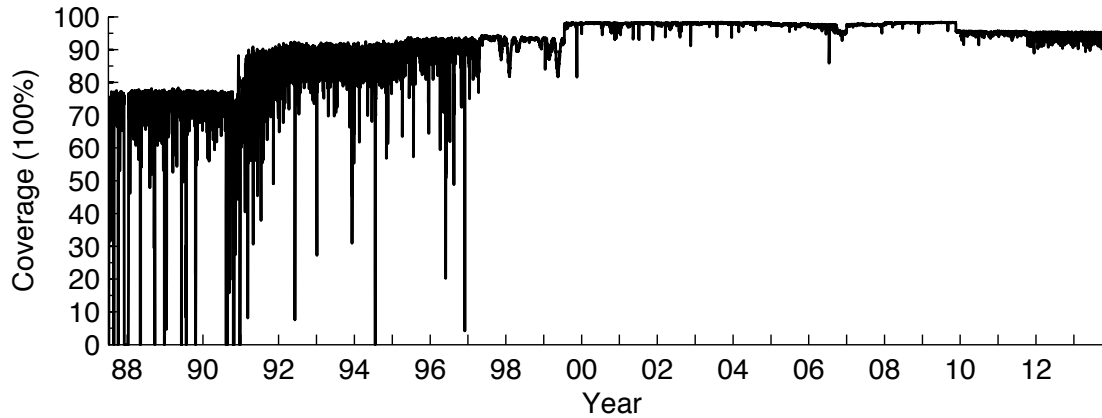


Figure 6. (a) Percentage of the global daily coverage on six hourly and daily for the sensor combination occurred during the 25-year period. (b) Time series of the percentage of the global daily coverage when all available sensors are combined.

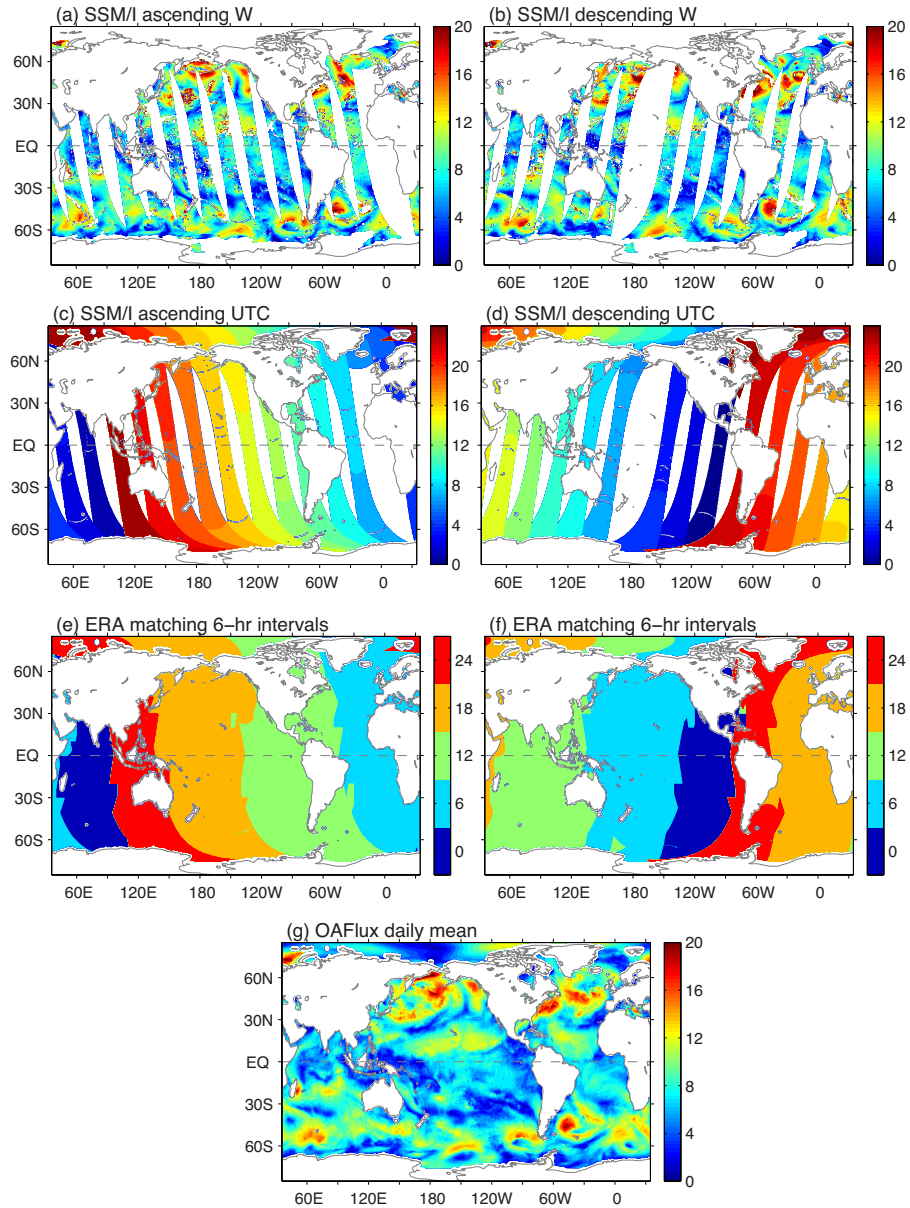


Figure 7. Illustration of the gap filling approach using the date of 1 January 1990 as an example.

(a) and (b) are SSMI F08 wind speed fields acquired during the ascending and descending orbit passes, respectively. (c) and (d) show the SSMI observing time in UTC for the respective ascending and descending passes. (e) and (f) are the nearest ERA-interim six-hour intervals that are used to fill in the gaps in the two SSMI passes. (g) is the daily-mean field produced from the OAF flux daily synthesis.

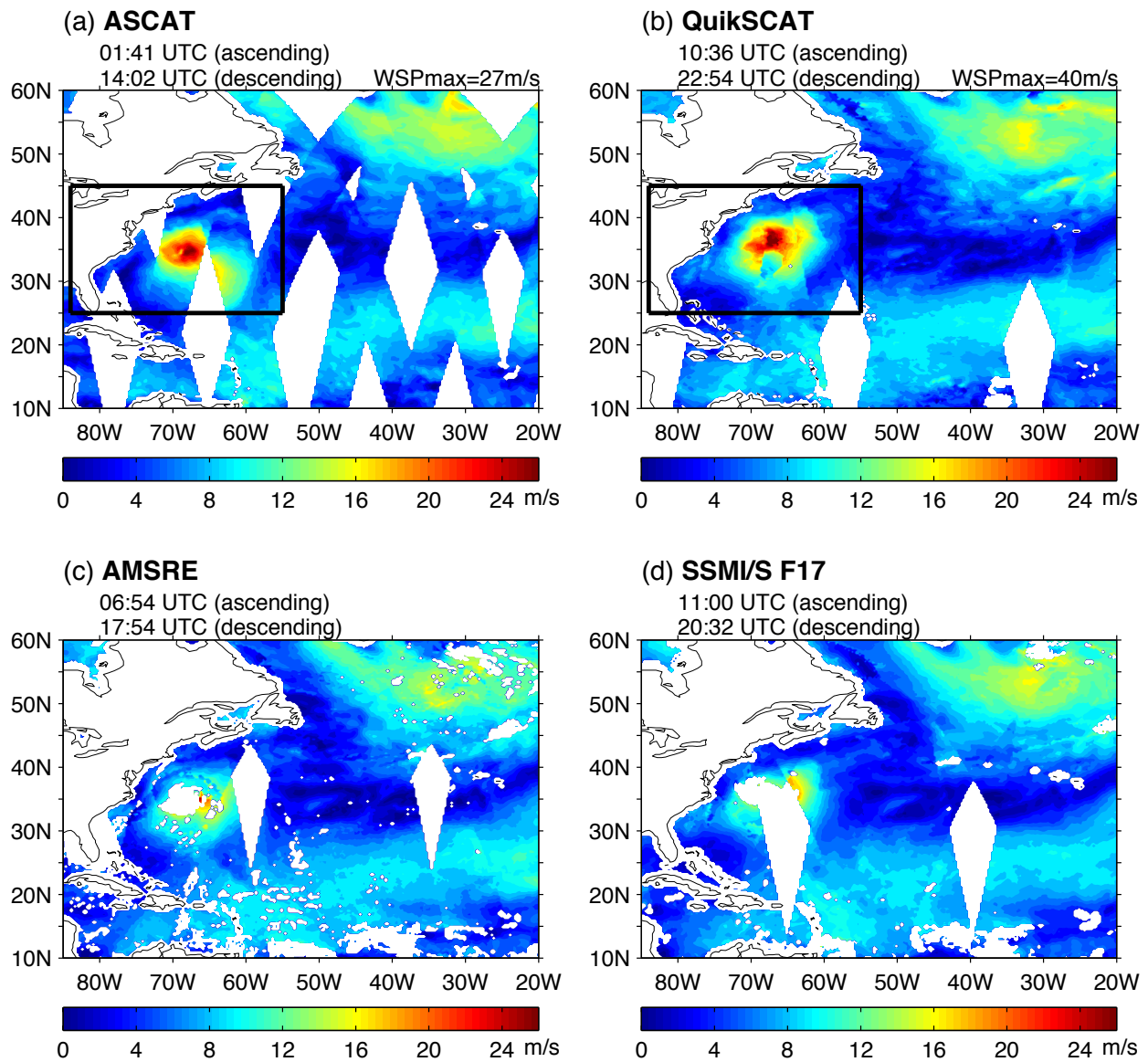


Figure 8. Wind speed retrievals on 22 August 2009, the day when Hurricane Bill moved to the northwest Atlantic. Daily coverage from combining ascending and descending passes is shown for (a) ASCAT, (b) QuikSCAT, (c) AMSRE-E, and (d) SSMIS F17. The square boxed region in (a) and (b) is the region of focus in Figure 7, in which wind convergence ($\partial u/\partial x + \partial v/\partial y$) is examined.

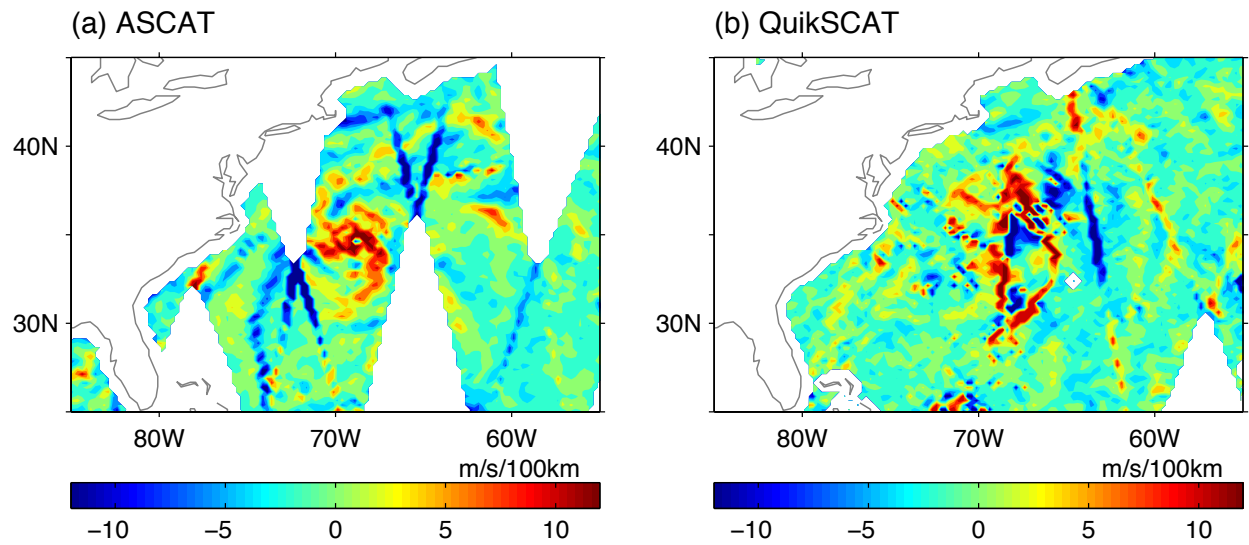


Figure 9. Wind convergence ($\partial u/\partial x + \partial v/\partial y$) constructed from (a) ASCAT and (b) QuikSCAT vector wind retrievals on 22 August 2009. The corresponding wind speed retrievals are shown in the boxed region in Figs. 8a-b, respectively.

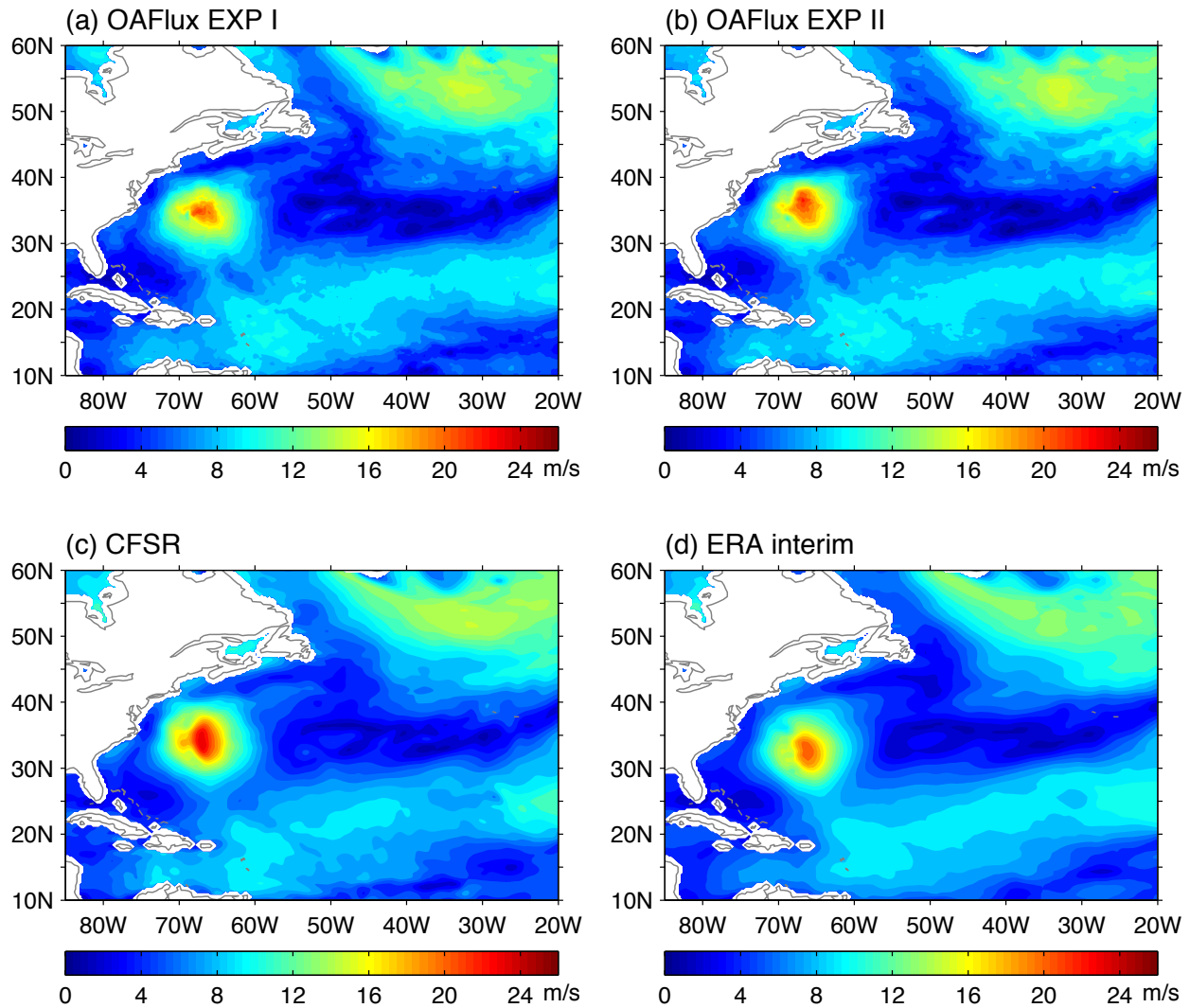


Figure 10. Daily-mean wind speed on 22 August 2009 from (a) OAFlex experiment I using ASCAT, SSMIS F17, and AMSRE; (b) OAFlex experiment II using QuikSCAT, SSMIS F17, and AMSRE; (c) NCEP1; and (d) ERA-interim. The two OAFlex experiments were to test the effect of inter-scatterometer differences in constructing the daily mean surface wind field.

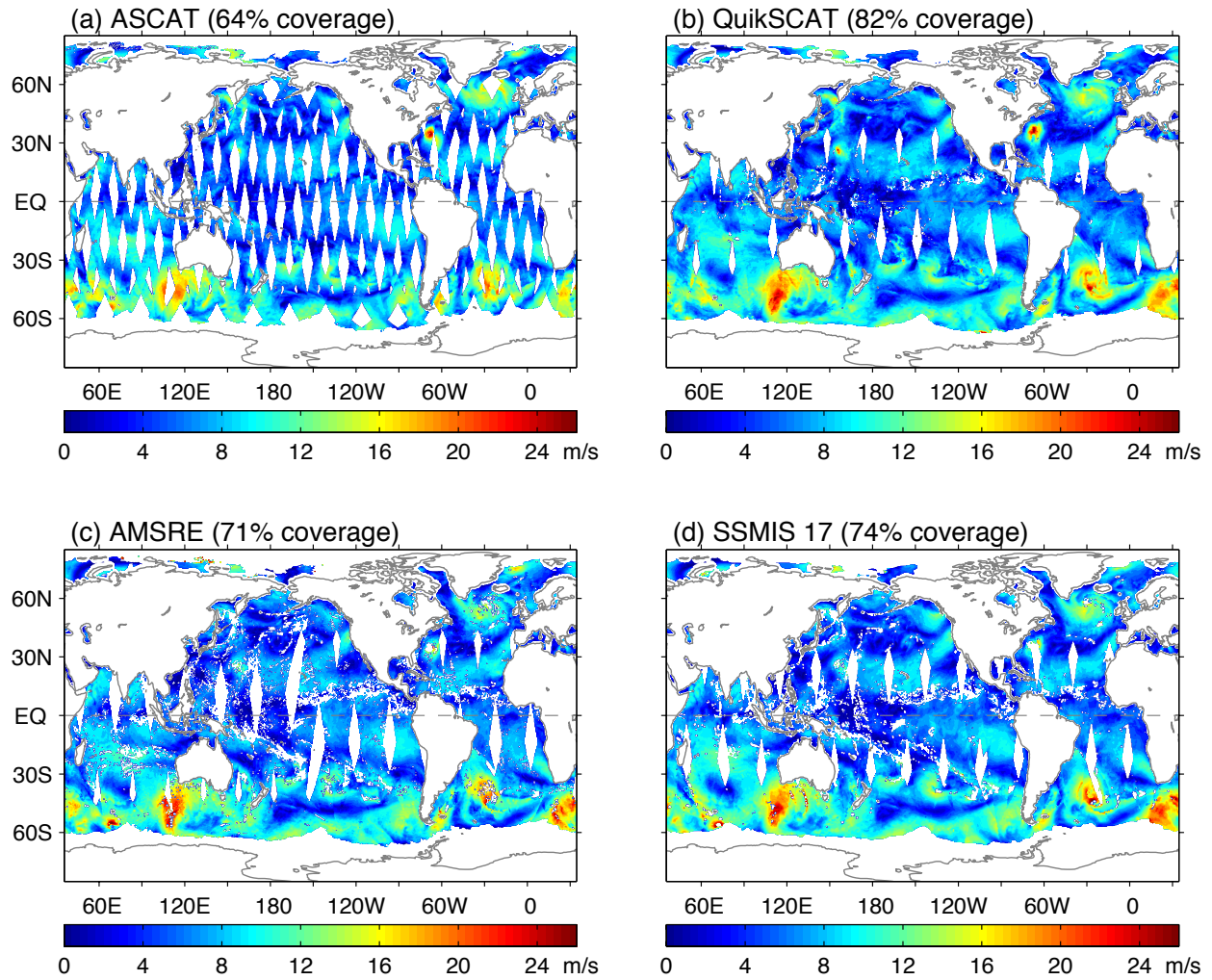


Figure 11. Global daily-mean wind speed field on 22 August 2009 from (a) ASCAT, (b) QuikSCAT, (c) AMSRE, and (d) SSMIS. All fields were constructed from summing up the ascending and descending passes.

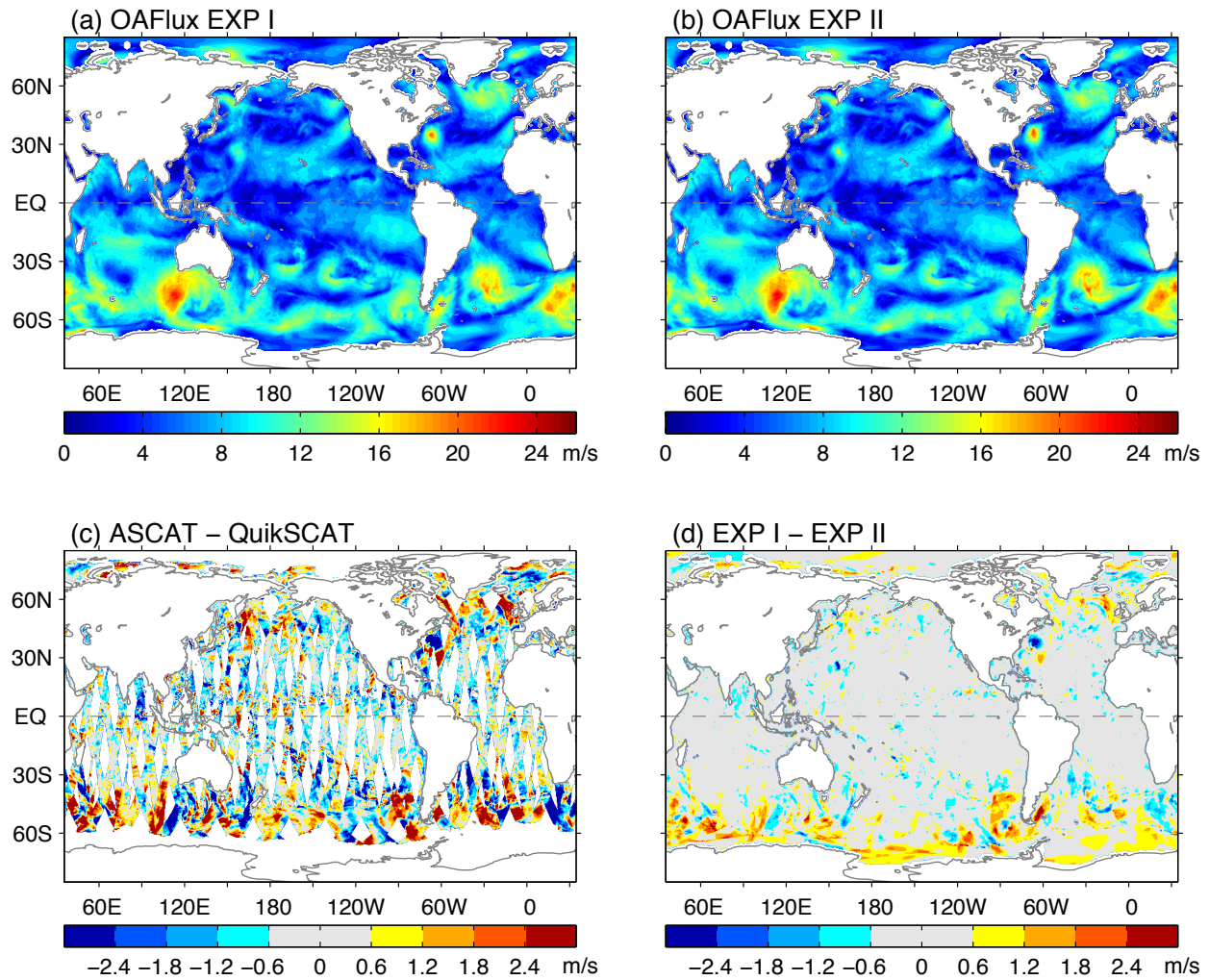
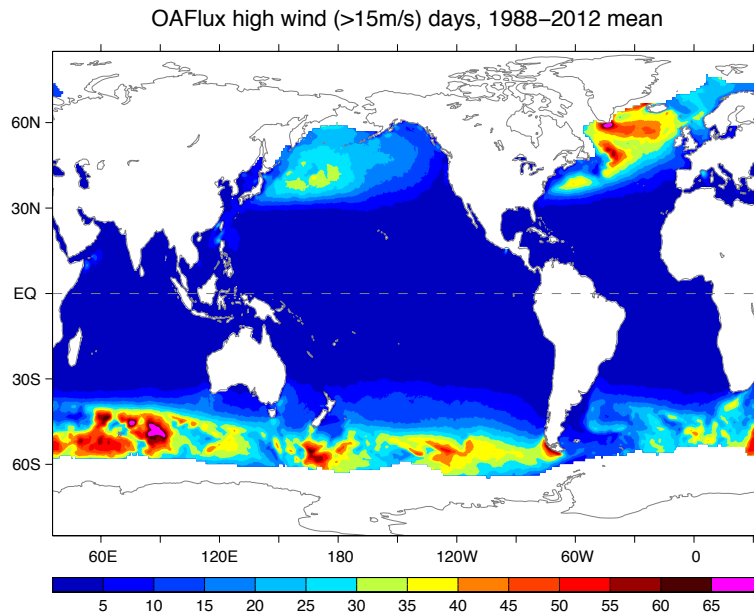


Figure 12. Global daily-mean wind speed field on 22 August 2009 from (a) OAFflux experiment I using ASCAT, SSMIS F17, and AMSRE; (b) OAFflux experiment II using QuikSCAT, SSMIS F17, and AMSRE; (c) wind speed differences between ASCAT and QuikSCAT; and (d) wind speed differences between the two OAFflux experiments.

(a)



(b)

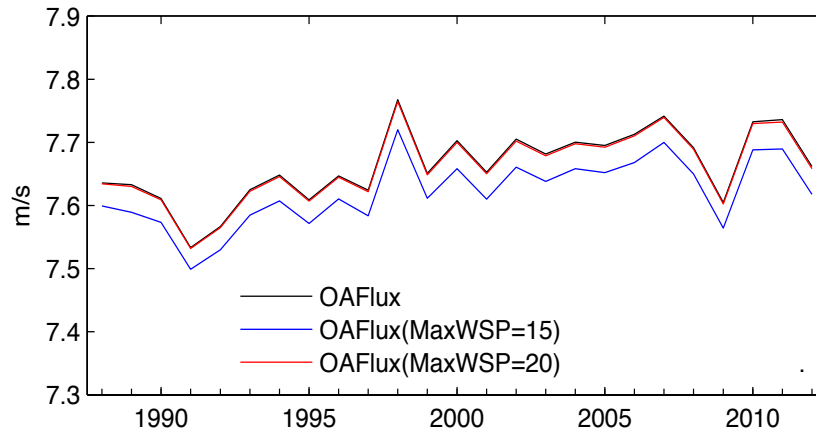


Figure 13. (a) Global distribution of the number of days that wind speeds exceed 15ms^{-1} per year constructed from SSMI and SSMIS sensors during the 25-year (1988-2012) period. (b) Three sets of annual-mean time series of globally averaged wind speeds: the full range (black), setting wind speeds greater than 15ms^{-1} to 15ms^{-1} (blue), and setting wind speeds greater than 20ms^{-1} to 20ms^{-1} (red).

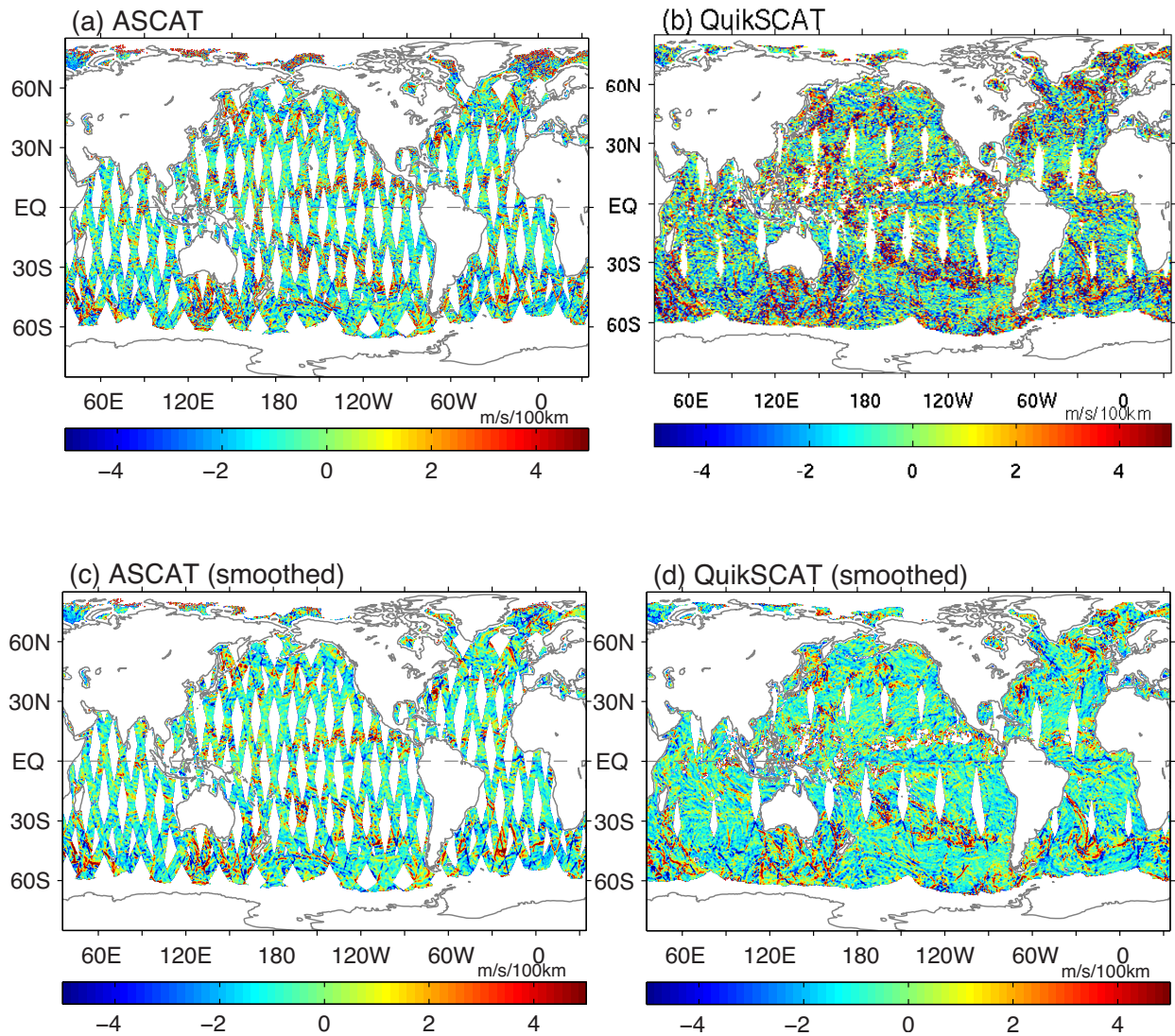


Figure 14. Near-surface wind convergence/divergence on 22 August 2009 constructed from (a) ASCAT retrievals, (b) QuikSCAT retrievals, (c) ASCAT retrievals after twice smoothed using a 1-2-1 spatial filter, and (d) QuikSCAT retrievals after twice smoothed using a 1-2-1 spatial filter. Positive values denote convergence and negative values denote divergence.

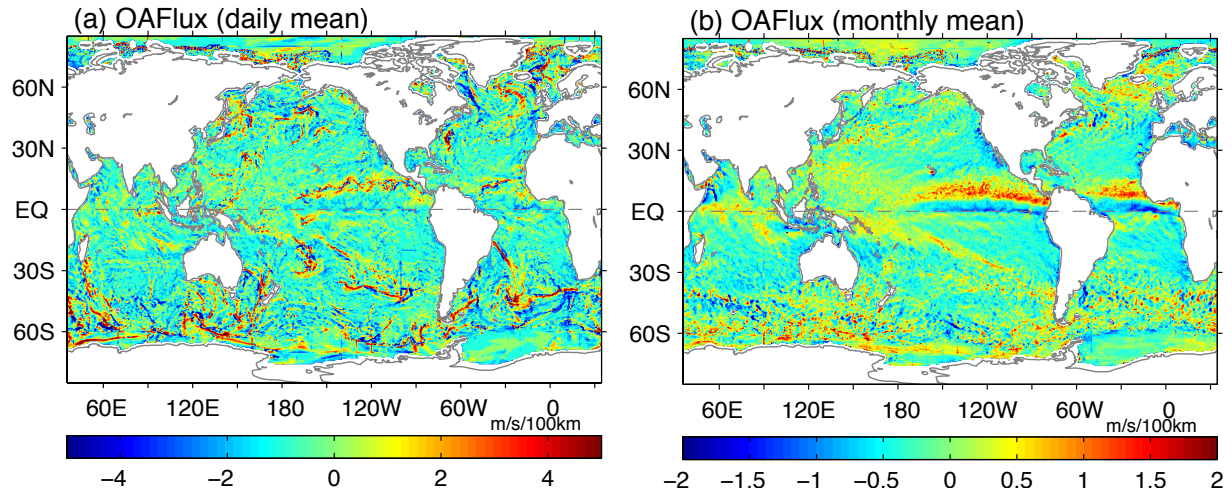


Figure 15. Near-surface wind convergence/divergence constructed from OAF flux (a) for daily mean on 22 August 2009, and (b) for the monthly mean averaged for August 2009. Positive values denote convergence and negative values denote divergence. Note the change of the colorbar scale between the two plots.

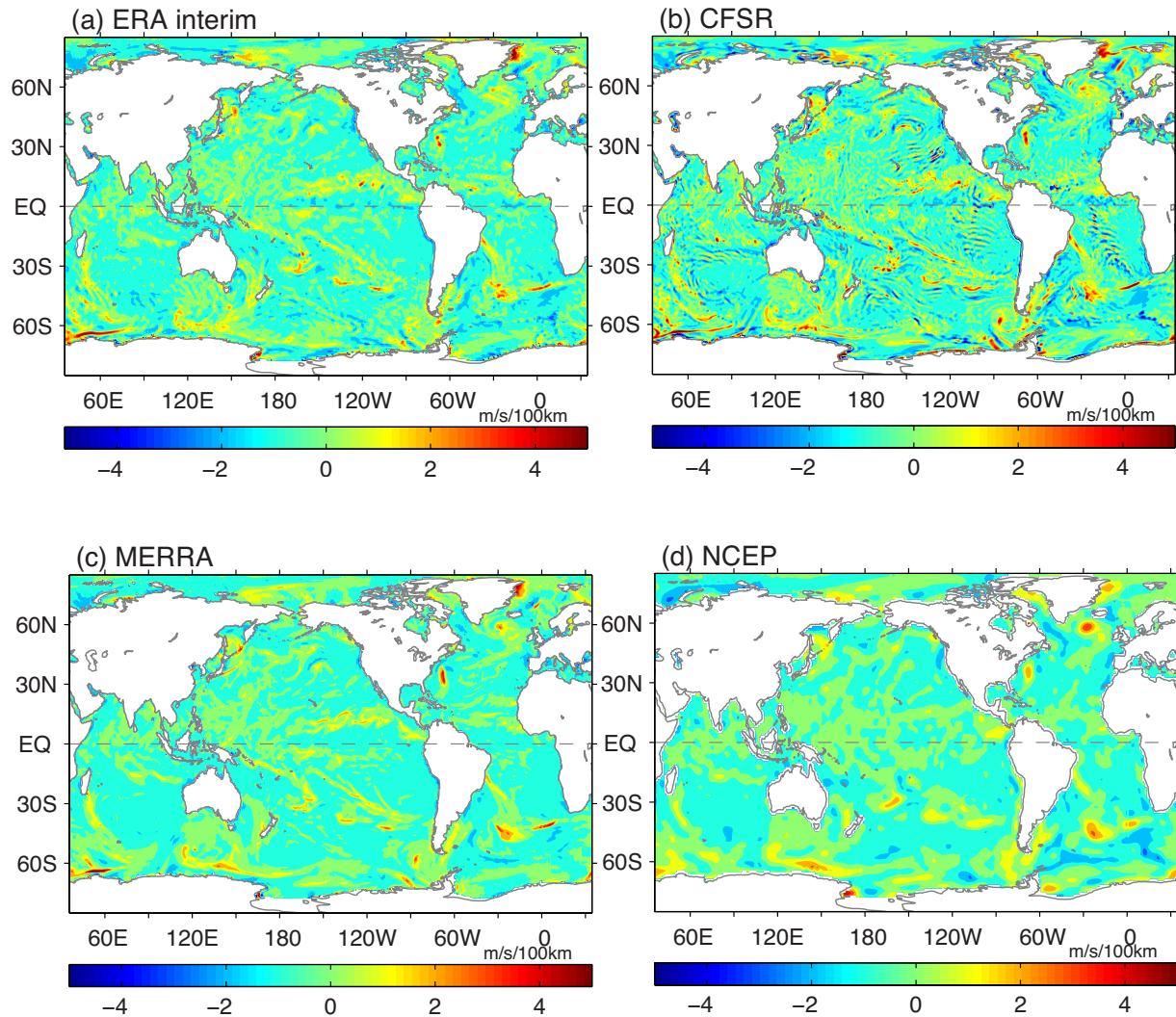


Figure 16. Near-surface wind convergence/divergence on 22 August 2009 constructed from (a) ERAinterim, (b) CFSR, (c) MERRA, and (d) NCEP1. Positive values denote convergence and negative values denote divergence.

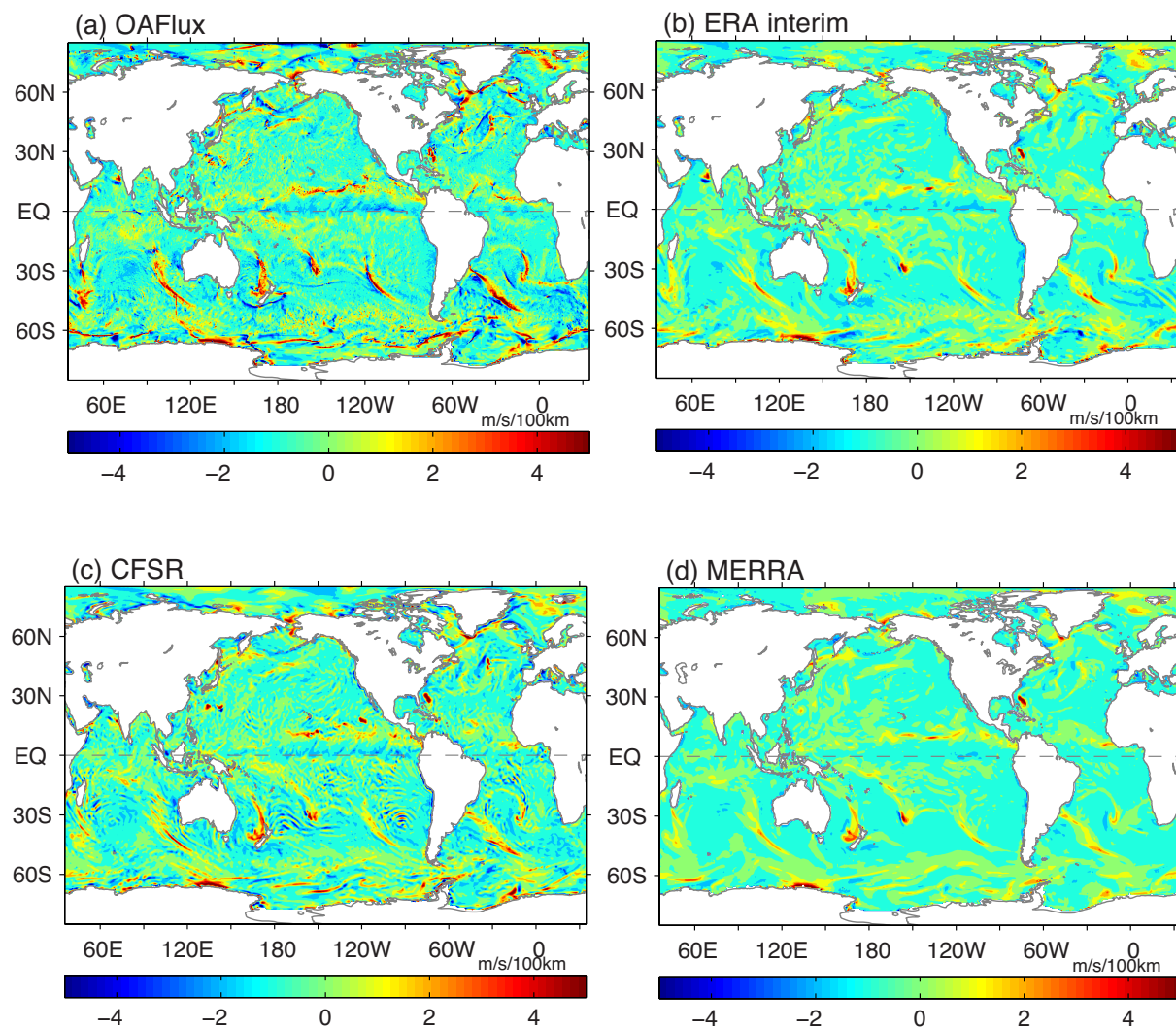


Figure 17. Near-surface wind convergence/divergence on 25 August 1998 constructed from (a) OAFlux, (b) ERAinterim, (c) CFSR, and (d) MERRA. Positive values denote convergence and negative values denote divergence. There was no scatterometer included in OAFlux.

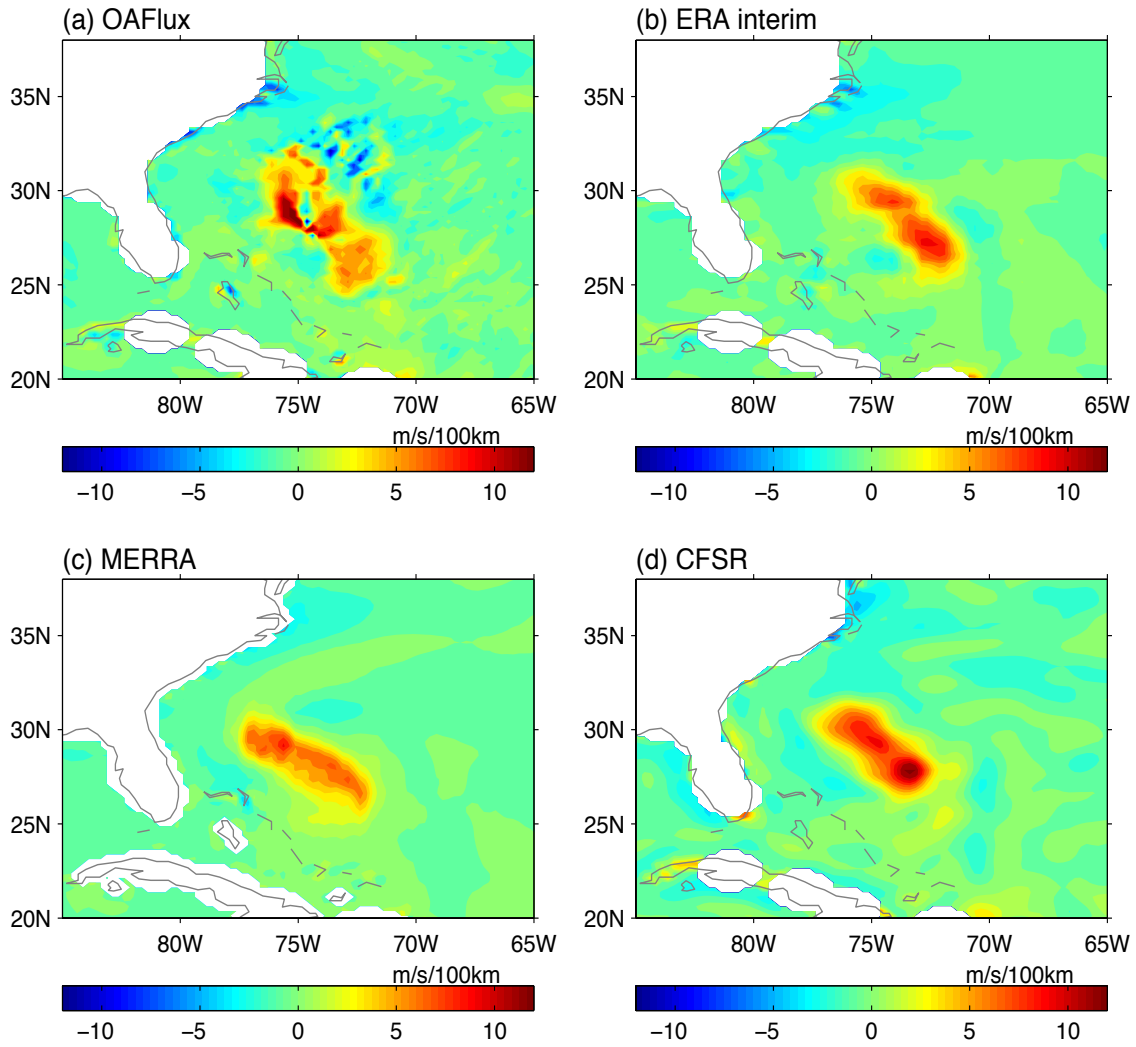


Figure 18. Near-surface wind convergence/divergence associated with Hurricane Bonnie on 25 August 1998 from (a) OAFlex, (b) ERAinterim, (c) MERRA, and (d) CFSR. Positive values denote convergence and negative values denote divergence.